A Bi-variant Variational Model for Diffeomorphic Image Registration with Relaxed Jacobian Determinant Constraints

Yanyan Li[a], Ke Chen[b], Chong Chen[c] and Jianping Zhang[a,d,*]

[a]*School of Mathematics and Computational Science, Xiangtan University, Xiangtan, 411105, Hunan, P. R. China*
[b]*Centre for Mathematical Imaging Techniques and Department of Mathematical Sciences, University of Liverpool, Liverpool, L6972L, Merseyside, United Kingdom*
[c]*LSEC, Institute of Computational Mathematics, Chinese Academy of Sciences, Beijing, 100190, Beijing, P. R. China*
[d]*National Center for Applied Mathematics in Hunan, Xiangtan University, Xiangtan, 411105, Hunan, P. R. China*

ARTICLE INFO

Keywords:
Diffeomorphic image registration
Jacobian soft constraints
Bi-variant optimization
Multilevel method
Alternative iterative minimization

ABSTRACT

Diffeomorphic registration has become a powerful approach for seeking a smooth and invertible spatial transformation between two coordinate systems which have been measured via the template and reference images. While the pointwise volume-preserving constraint $\det(\nabla\boldsymbol{\varphi}(\boldsymbol{x})) = 1$ is effective for some problems, it is too stringent for many other problems especially when the local deformations are relatively large, because it may lead to a poor large-deformation for enforcing local matching. In this paper, we propose a novel bi-variant diffeomorphic image registration model with the soft constraint of Jacobian equation $\det(\nabla\boldsymbol{\varphi}(\boldsymbol{x})) = f(\boldsymbol{x}) > 0$, which allows local deformations to shrink and grow in a flexible range $0 < \kappa_m < \det(\nabla\boldsymbol{\varphi}(\boldsymbol{x})) < \kappa_M$. The Jacobian determinant of the transformation is explicitly controlled by optimizing the relaxation function $f(\boldsymbol{x})$. To prevent deformation folding and enhance the smoothness of deformation, we not only impose a positivity constraint in optimizing the relaxation function $f(\boldsymbol{x})$, but also employ a regularizer to ensure the smoothness of $f(\boldsymbol{x})$. Furthermore, the positivity constraint ensures that $f(\boldsymbol{x})$ is as close to one as possible, which helps to obtain a volume-preserving transformation on average. We further analyze the existence of the minimizer for the variational model and propose a penalty splitting method with a multilevel strategy to solve this model. Numerical experiments show that the proposed algorithm is convergent, and the positivity constraint can control the range of relative volume and not compromise registration accuracy. Moreover, the proposed model produces diffeomorphic maps for large deformation, and achieves better performance compared to the several existing registration models.

1. Introduction

Image registration is the process that attempts to seek an optimal transformation between two or more images to establish a geometric correspondence. In the last few decades, a great number of popular registration models have been developed to obtain reasonable transformations, including total variation (TV) model [23, 35], modified total variation (MTV) model [12], total fractional variation (TFV) model [58, 27], diffusion model [19, 37], curvature model [20, 21, 29], elastic model [22], viscous fluid model [11, 15], and optical flow model [32]. Although these registration models can generate smooth transformations for relatively small deformations, not all models are effective for large deformations. But, few models can be guaranteed to generate the diffeomorphic mappings.

The diffeomorphic demons algorithm works in the space of diffeomorphisms to enforce the transformation invertibility. Vercauteren et al. [1, 50] shown that the demons algorithm [48] can be extended to represent the complete spatial transformation in the log-domain. Yeo et al. [54] proposed the spherical demons method based

---
*Corresponding author

✉ jpzhang@xtu.edu.cn (J. Zhang)
ORCID(s): 0000-0001-7141-9464 (J. Zhang)

on the mean curvature and average convexity to transform image surface. In addition, the large deformation diffeomorphic metric mapping (LDDMM) [17, 5] is a popular registration framework, which can handle large deformation and generate diffeomorphic transformation. Based on the LDDMM framework and shape analysis, Charon et al. proposed a generalization of registration algorithms to non-oriented shapes [7] and an extension of diffeomorphic registration to enable a morphological analysis of data structures with inherent density variations and imbalances [34]. C. Chen [8] employed diffeomorphic optimal transportation that combines the Wasserstein distance and the flow of diffeomorphisms, to build a joint image reconstruction and motion estimation model, which is suitable for spatiotemporal imaging involving mass-preserving large diffeomorphic deformations. Bauer et al. [4] proposed diffeomorphic density matching by optimal information transport and applied it to medical image registration, building on connections between the Fisher–Rao information metric on the space of probability densities and right-invariant metrics on the infinite-dimensional manifold of diffeomorphisms. Feydy et al. [18] introduced a non-local geometric similarity measure based on unbalanced optimal transport methods and fast entropic solvers to achieve robust and simple diffeomorphic registration. We also refer the readers to [2, 5, 9, 10, 28, 36, 41, 46] for more details.

Several registration models have been developed to avoid mesh folding by restricting the Jacobian determinant quantity $\det(\nabla\boldsymbol{\varphi})$ of the transformation $\boldsymbol{\varphi}$. Haber and Modersitzki [25] proposed an elastic registration model subject to pointwise volume-preserving by restricting $\det(\nabla\boldsymbol{\varphi}) = 1$, which can ensure that the mapping is diffeomorphic. Although such incompressibility has important applications in some fields, it is not necessary or reasonable in others. To generate a more reasonable and practical mapping, Haber and Modersitzki then proposed to relax the Jacobian determinant constraint into a certain interval $0 < \kappa_m < \det(\nabla\boldsymbol{\varphi}) < \kappa_M$ [26]. Lam and Lui [38, 39] introduced a novel model involving a Beltrami coefficient term to obtain diffeomorphic image registration via quasi-conformal maps. One of the most important features of this method is that the deformed Jacobian determinant can be represented by the Beltrami coefficient. As pointed out, if the infinite norm of the Beltrami coefficient is less than 1, thus the Jacobian determinant is greater than 0, so that such model can deal with large deformation.

It is possible to reformulate the diffeomorphic image registration into a variational problem with an additional penalty term relating to the deformed Jacobian determinant. Burger et al. [6] explicitly monitored $\det(\nabla\boldsymbol{\varphi})$ using an unbiased function in the hyper-elastic model to ensure that the deformation is diffeomorphic. Rühaak et al. [47] introduced a volume penalty function to control the change of $\det(\nabla\boldsymbol{\varphi})$, which prevented the formation of foldings by keeping the $\det(\nabla\boldsymbol{\varphi})$ positive. Yanovsky et al. [52, 53] applied the symmetric Kullback–Leibler (sKL) distance to quantify the deformation for seeking an unbiased diffeomorphic mapping. Some other work also involved controlling $\det(\nabla\boldsymbol{\varphi})$ by penalty functions [30, 56, 57].

In general, there are three main approaches for obtaining diffeomorphic maps. One approach is to find deformation on the manifold of diffeomorphisms. An advantage of the method is computationally efficiency, but it does not control the geometric properties of the deformation field and may result in deformation that is close to being nondiffeomorphic. The second approach is to prevent nondiffeomorphic mappings by adding additional constraints that equivalent to $\det(\nabla\boldsymbol{\varphi}) > 0$. This method can control the deformation explicitly and obtain the diffeomorphic mappings without manual intervention. However, this may cause either over-preservation of volume or the volume change to be large, resulting in mismatches or inaccurate registration. The third approach is to indirectly control $\det(\nabla\boldsymbol{\varphi})$ via Beltrami (or Beltrami-like in 3D) coefficient. The advantage of this method is that it can deal with large deformations well and obtain smooth deformations. However, this method works on the Beltrami coefficient and deformation simultaneously, making the structure of energy functional too complex and resulting in high computational expense, and convergence of the method cannot also be guaranteed.

Recently, deep learning-based methods have attracted considerable attention in image registration. Yuchen Guo et al. [24] proposed a framework for the automatic landmark detection and registration of brain cortical surfaces using quasi-conformal geometry and convolutional neural networks. Dongming Wei et al. [51] proposed a recurrently usable deep neural network for infant brain MR image registration. Tony et al. [43] proposed a novel, efficient unsupervised symmetric image registration method that maximizes the similarity between images in the space of diffeomorphic maps and estimates both forward and inverse transformations simultaneously.

Deep learning-based methods harnesses the inductive capabilities of neural networks on the data set, shifting the continuous iterative optimization inherent in traditional methods to the training process of deep learning. As a result, deep learning-based image registration methods significantly outperform traditional methods in terms of registration efficiency. However, deep learning-based methods lack rigorous mathematical theoretical support, which limits their interpretability. Furthermore, it has poor processing capacity for large deformation registration and is not guaranteed to generate diffeomorphism transformations [16]. In contrast, the traditional image registration methods offer rigorous mathematical theoretical support and use precise mathematical expressions to guide the registration process. It also has achieved success in large deformation registration and in maintaining diffeomorphism. Although there are many research achievements on traditional registration methods, their registration accuracy and efficiency (especially for 3D problems) still cannot meet people's needs. The construction of a new diffeomorphic registration model and the design of a highly accurate and fast registration algorithm still face many difficulties and challenges.

In this work, we aim to reformulate a novel bi-variant diffeomorphic registration approach that uses a variational minimization model, also provide an existence result of the minimizer for the variational model. This approach generates smooth and invertible transformation, and the proposed model can be effectively applied to large deformation registration. Our contributions are summarized as follows.

1. We propose an image registration framework that imposes a soft constraint of Jacobian equation $\det(\nabla \boldsymbol{\varphi}(\boldsymbol{x})) = f(\boldsymbol{x})$ with a flexible function $f(\boldsymbol{x}) > 0$ as a constraint, which can generate diffeomorphic mapping $\boldsymbol{\varphi}(\boldsymbol{x})$ by optimizing the positive function $f(\boldsymbol{x})$ that allows local deformations to shrink and grow in a flexible range without compromising registration accuracy for large deformation.

2. We provide a positivity penalty term $\int_\Omega \phi(f(\boldsymbol{x})) d\boldsymbol{x}$ that could be integrated into the registration model to optimize $f(\boldsymbol{x})$ automatically. The control function $\boldsymbol{\phi}(\cdot)$ is employed to enforce $f(\boldsymbol{x}) > 0$ as close to one as possible. Furthermore, the regularization term $\int_\Omega |\nabla f(\boldsymbol{x})|^2 d\boldsymbol{x}$ is used to optimize the smoothness of $f(\boldsymbol{x})$, which can indirectly improve the smoothness of transformation $\boldsymbol{\varphi}(\boldsymbol{x})$, and the existence of the optimal solution of our model is theoretically guaranteed.

3. We design a penalty splitting algorithm with a multilevel strategy to solve the bi-variant variational model. Numerical experiments show that the proposed algorithm is convergent, which not only controls the range of $\det(\nabla \boldsymbol{\varphi}(\boldsymbol{x}))$ but also does not compromise registration accuracy. Moreover, the proposed model can produce diffeomorphic maps for large deformation and achieve better performance compared to the several existing registration models.

The rest of the paper is organized as follows. In Section 2, we review several popular models related to the diffeomorphic image registration. In Section 3, we give the mathematical analysis and solving algorithm of the newly proposed registration model. The numerical implementation of the proposed model is presented in Section 4. We present 2D and 3D examples to evaluate the performance of our approach in Section 5. Finally, we summarize this work in Section 6.

2. Reviews

Given a pair of images $T(\cdot), R(\cdot) : \Omega \subset \mathbb{R}^d \to \mathbb{R}$ ($d = 2$ or 3), the aim of image registration is to seek a suitable transformation $\bar{\boldsymbol{\varphi}}(\cdot) : \mathbb{R}^d \to \mathbb{R}^d$ that satisfies $T(\bar{\boldsymbol{\varphi}}(\boldsymbol{x})) \approx R(\boldsymbol{x})$. The updated transformation $\bar{\boldsymbol{\varphi}}(\boldsymbol{x})$ will be described by simply adding the displacement field $\boldsymbol{u}(\boldsymbol{x})$ into the current transformation $\boldsymbol{\varphi}(\boldsymbol{x})$, i.e., $\bar{\boldsymbol{\varphi}}(\boldsymbol{x}) = \boldsymbol{\varphi}(\boldsymbol{x}) + \boldsymbol{u}(\boldsymbol{x})$. To make the deformed image $T(\bar{\boldsymbol{\varphi}}(\boldsymbol{x}))$ closer to the reference image $R(\boldsymbol{x})$, the similarity measure $\mathcal{D}(\boldsymbol{u})$ of image registration can be minimized as

$$\min_{\boldsymbol{u}} \left\{ \mathcal{D}(\boldsymbol{u}) := \frac{1}{2} \int_\Omega \left[T(\boldsymbol{\varphi}(\boldsymbol{x}) + \boldsymbol{u}(\boldsymbol{x})) - R(\boldsymbol{x}) \right]^2 d\boldsymbol{x} \right\}. \tag{1}$$

A simple optimization of (1) leads to an ill-posed problem with unstable and nonsmooth solutions [25]. Hence a regularizer $\mathcal{F}(\cdot)$ is added to construct the well-posed problem

$$\min_{\boldsymbol{u}} \left\{ \mathcal{J}(\boldsymbol{u}) := \mathcal{D}(\boldsymbol{u}) + \tau \mathcal{F}(\boldsymbol{u}) \right\}, \tag{2}$$

where $\tau > 0$ is a constant to balance $\mathcal{D}(\boldsymbol{u})$ and $\mathcal{F}(\boldsymbol{u})$. We refer readers to [31, 44, 14] for many classical similarity measures, and [13, 19, 20, 22, 58, 59, 61] for the popular regularizers in image registration.

The diffeomorphism of the mapping $\bar{\boldsymbol{\varphi}} = \boldsymbol{\varphi} + \boldsymbol{u}$ is a significant requirement in image registration, and it can be translated into its necessary condition $\mathcal{K}(\boldsymbol{u}(\boldsymbol{x})) = \det(\nabla\bar{\boldsymbol{\varphi}}) > 0$. A natural technique is to achieve $\mathcal{K}(\boldsymbol{u}(\boldsymbol{x})) > 0$ as a positivity constraint to explicitly safeguard against nondiffeomorphic mapping $\bar{\boldsymbol{\varphi}}$ when minimizing the functional $\mathcal{J}(\boldsymbol{u})$. Therefore, the constrained model can be written as

$$\min_{\boldsymbol{u}} \left\{ \mathcal{J}(\boldsymbol{u}) = \mathcal{D}(\boldsymbol{u}) + \tau \mathcal{F}(\boldsymbol{u}) \right\},$$
$$\text{s.t.} \quad \mathcal{K}(\boldsymbol{u}(\boldsymbol{x})) = \det\left(\nabla(\boldsymbol{\varphi} + \boldsymbol{u})\right) > 0, \ \forall \boldsymbol{x} \in \Omega. \tag{3}$$

Before introducing our model, we review several recent work that imposes the Jacobian determinant positivity constraint $\det\left(\nabla(\boldsymbol{\varphi} + \boldsymbol{u})\right) > 0$ in some indirect ways.

- Haber and Modersitzki [25] proposed a pointwise volume-preserving image registration model, which is followed by

$$\min_{\boldsymbol{u}} \left\{ \mathcal{J}(\boldsymbol{u}) = \mathcal{D}(\boldsymbol{u}) + \frac{\tau}{2} \int_{\Omega} \left[\mu\|\nabla\boldsymbol{u}\|^2 + (\lambda + \mu)(\nabla \cdot \boldsymbol{u})^2\right] d\boldsymbol{x} \right\},$$
$$\text{s.t.} \quad \mathcal{K}(\boldsymbol{u}(\boldsymbol{x})) = 1, \ \forall \boldsymbol{x} \in \Omega, \tag{4}$$

  where λ and μ are the so-called Lamé constants. However, the pointwise volume preservation is not desirable when the anatomical structure is compressible in medical imaging, so a soft inequality constraint that allows local regions of the image to shrink or grow within a specified range is more practical.

- Modersitzki et al. [26] then proposed the relaxed constraint to improve the registration model (4), namely,

$$\min_{\boldsymbol{u}} \left\{ \mathcal{J}(\boldsymbol{u}) = \mathcal{D}(\boldsymbol{u}) + \frac{\tau}{2} \int_{\Omega} \left[\mu\|\nabla\boldsymbol{u}\|^2 + (\lambda + \mu)(\nabla \cdot \boldsymbol{u})^2\right] d\boldsymbol{x} \right\},$$
$$\text{s.t.} \quad \kappa_m \leq \mathcal{K}(\boldsymbol{u}(\boldsymbol{x})) \leq \kappa_M, \ \forall \boldsymbol{x} \in \Omega, \tag{5}$$

  where the positive constants κ_m and κ_M are provided by the user as prior information in the specific application. In particular, when $\kappa_m = \kappa_M = 1$, the model (5) degenerates to pointwise volume preserving image registration (4).

- Yanovsky et al. [53] applied the symmetric Kullback-Leibler (sKL) distance to propose a log-unbiased fluid image registration model as follow

$$\min_{\boldsymbol{u}} \left\{ \mathcal{J}(\boldsymbol{u}) = \mathcal{D}(\boldsymbol{u}) + \lambda \int_{\Omega} \left(|\mathcal{K}(\boldsymbol{u}(\boldsymbol{x}))| - 1\right) \log\left(|\mathcal{K}(\boldsymbol{u}(\boldsymbol{x}))|\right) d\boldsymbol{x} \right\}, \tag{6}$$

where $\lambda > 0$ is the regularization parameter. The corresponding Euler-Lagrange equation can be written as

$$g(x, u) := [T(\varphi + u) - R(x)]\nabla T$$

$$- \lambda \begin{bmatrix} -\frac{\partial}{\partial x_1}\left(\frac{\partial(\varphi_2+u_2)}{\partial x_2}L'\right) + \frac{\partial}{\partial x_2}\left(\frac{\partial(\varphi_2+u_2)}{\partial x_1}L'\right) \\ \frac{\partial}{\partial x_1}\left(\frac{\partial(\varphi_1+u_1)}{\partial x_2}L'\right) - \frac{\partial}{\partial x_2}\left(\frac{\partial(\varphi_1+u_1)}{\partial x_1}L'\right) \end{bmatrix} = 0,$$

where $L' = 1 + \log\left(|\mathcal{K}(u(x))|\right) - 1/|\mathcal{K}(u(x))|$. The authors use the idea of [15] obtaining the instantaneous velocity $v = -G_\sigma * g$ from the Gaussian kernel $G_\sigma * g$ (σ is variance) of functional g, then the displacement field u is obtained by solving the material derivative of u as follows

$$\begin{cases} \frac{\partial u}{\partial t} + (\nabla u)v = v, \\ u(x, 0) = 0. \end{cases}$$

The above log-unbiased registration can help to obtain an unbiased diffeomorphic transformation. Also see [52] for more details.

- Burger et al. [6] used a penalty function $\phi(z) = \left((z-1)^2/z\right)^2$ to control $\det(\nabla\bar{\varphi}(x))$ such that its shrinkage and growth have the same price due to $\phi(1/z) = \phi(z)$. Then the penalty term of hyper-elastic registration can be written as

$$\mathcal{F}(u) = \int_\Omega \left(\frac{(\mathcal{K}(u(x)) - 1)^2}{\mathcal{K}(u(x))}\right)^2 dx, \tag{7}$$

where one can explicitly show that the deformation is physically meaningful due to $\mathcal{F}(u) \rightarrow \infty$ for $\mathcal{K}(u(x)) \rightarrow 0$.

- Rühaak et al. [47] also directly measured the change of $\mathcal{K}(u(x))$ by adding the volume change control term $\int_\Omega \phi\left(\mathcal{K}(u(x))\right)dx$ in the energy functional, and ϕ was defined as

$$\phi(z) = \begin{cases} \frac{(z-1)^2}{z} & \text{if } z > 0, \\ +\infty & \text{otherwise.} \end{cases} \tag{8}$$

- Zhang and Chen [56] proposed a Beltrami coefficient-based regularizer $\mathcal{F}(u)$ to seek a diffeomorphic mapping $\bar{\varphi} = \varphi + u$, which was defined as

$$\mathcal{F}(u) = \int_\Omega \phi(|\mu|^2)dx, \text{ with } |\mu|^2 = \frac{\|\nabla(\varphi + u)\|^2 - 2\mathcal{K}(u(x))}{\|\nabla(\varphi + u)\|^2 + 2\mathcal{K}(u(x))}, \tag{9}$$

where $\phi(z) = \frac{z}{(z-1)^2}$ or $\frac{z^2}{(z-1)^2}$.

3. The proposed image registration model

In this part, we first introduce the proposed diffeomorphic registration model, which can be potentially applied to large deformation. We then give the mathematical analysis including the existence of the optimal solution of our bi-variant variational model, and derive an optimization scheme to solve the proposed variational framework.

3.1. Proposed model

As described above, we can prevent folding of the transformation $\bar{\boldsymbol{\varphi}}$ by restricting the Jacobian determinant $\det\left(\nabla\bar{\boldsymbol{\varphi}}(\boldsymbol{x})\right) > 0$. We propose to construct diffeomorphic model by taking the Jacobian equation $\det\left(\nabla\bar{\boldsymbol{\varphi}}(\boldsymbol{x})\right) = f(\boldsymbol{x})$ as a constraint, and maintaining the Jacobian determinant positive is equal to keeping the unknown relaxation function $f(\boldsymbol{x}) > 0$. Our new idea is to design a model that can allow $f(\boldsymbol{x})$ to be flexible and yet ensures $f(\boldsymbol{x})$ remain positive. This way, our new model is much simpler than similar models in the literature and is equally effective. Therefore, the proposed diffeomorphic registration model can be written as

$$
\min_{\boldsymbol{u}\in\mathcal{V},\,0<f\in L^2(\Omega)} \left\{ \mathcal{D}(\boldsymbol{u}) + \frac{\tau_1}{2}\int_\Omega \|\nabla\boldsymbol{u}\|^2 d\boldsymbol{x} \right\},
$$
$$
\text{s.t.}\quad \mathcal{K}(\boldsymbol{u}(\boldsymbol{x})) = \det\left(\nabla(\boldsymbol{\varphi}+\boldsymbol{u})\right) = f(\boldsymbol{x}),\quad \forall\boldsymbol{x}\in\Omega,
$$

(10)

where $\mathcal{V}$ is defined by

$$
\mathcal{V} := \{\boldsymbol{v}\,\big|\,\boldsymbol{v}\in[\mathcal{H}^1(\Omega)]^d \text{ and } \boldsymbol{v}|_{\partial\Omega}=\boldsymbol{0}\}.
$$

Obviously, the positivity requirement of $f(\boldsymbol{x})$ in (10) is not easy to maintain during the optimization computation. To overcome this draw, we propose to combine a penalty term $\int_\Omega \phi(f(\boldsymbol{x}))d\boldsymbol{x}$ that can be integrated into (10), so that $f(\boldsymbol{x})$ can be automatically optimized. The registration model can be rewritten as

$$
\min_{\boldsymbol{u}\in\mathcal{V},\,f\in L^2(\Omega)} \left\{ \mathcal{D}(\boldsymbol{u}) + \frac{\tau_1}{2}\int_\Omega \|\nabla\boldsymbol{u}\|^2 d\boldsymbol{x} + \tau_2\int_\Omega \phi(f(\boldsymbol{x}))d\boldsymbol{x} \right\},
$$
$$
\text{s.t.}\quad \det\left(\nabla(\boldsymbol{\varphi}+\boldsymbol{u})\right) = f(\boldsymbol{x}),\quad \forall\boldsymbol{x}\in\Omega,
$$

(11)

where the control function $\phi(\cdot)$ is known and $\tau_2 > 0$.

Here we introduce two choices of function $\phi(\cdot)$. One choice is to consider the form in [47] as

$$
\phi_1(f) = \begin{cases} \frac{(f-1)^2}{f}, & \text{if } f > 0, \\ +\infty, & \text{otherwise.} \end{cases}
$$

Note that $\phi_1(f)$ is minimized when $f(\boldsymbol{x}) = 1$. Therefore, the penalty term $\int_\Omega \phi(f(\boldsymbol{x}))d\boldsymbol{x}$ in (11) can prevent the formation of folding by keeping $f(\boldsymbol{x}) > 0$, and $f(\boldsymbol{x})$ is explicitly monitored because the control term will be infinity when $f(\boldsymbol{x}) \leq 0$. Another choice is inspired by the work of log-unbiased image registration [53] that associates deformations with their corresponding global density maps, in general, it applies the sKL distance to quantify the magnitude of deformations. We propose to measure the magnitude of $f(\boldsymbol{x})$ by means of the sKL distance between $f(\boldsymbol{x})$ and 1, namely,

$$
\phi_2(f) = \begin{cases} (f-1)\log(f), & \text{if } f > 0, \\ +\infty, & \text{otherwise.} \end{cases}
$$

It is easy to know that the control function $\phi_2(f)$ is always non-negative, and its minimum is zero when $f(\boldsymbol{x}) = 1$. Similarly, $f(\boldsymbol{x}) \leq 0$ can also be explicitly restricted. As have been seen, the above choices can ensure that $f(\boldsymbol{x}) > 0$ for any $\boldsymbol{x} \in \Omega$ and $f(\boldsymbol{x})$ is as close to 1 as possible. It shows that the constraint condition $\det\left(\nabla\bar{\boldsymbol{\varphi}}(\boldsymbol{x})\right) = f(\boldsymbol{x})$ can indirectly restrict the range of the Jacobian determinant $\det\left(\nabla\bar{\boldsymbol{\varphi}}(\boldsymbol{x})\right)$ so that the deformation tends to be volume-preserving.

Finally, we add a diffusion regularizer for the positivity constraint $f(\boldsymbol{x})$ into model (11) to improve its smoothness. Let $\mathcal{M}(\Omega) = \{\boldsymbol{\omega} := (\boldsymbol{u}, f) \in \mathcal{V}(\Omega) \times \mathcal{W}(\Omega)\} \subset [\mathcal{H}^1(\Omega)]^d \times \mathcal{H}^1(\Omega) = [\mathcal{H}^1(\Omega)]^{d+1}$ denote the solution constraints where $\mathcal{W}(\Omega) := \{f(\boldsymbol{x}) | f \in \mathcal{H}^1(\Omega) \text{ and } f|_{\partial\Omega} = 1\}$, thus a novel bi-variant registration model for computing large diffeomorphic transformation is presented as

$$
\min_{(\boldsymbol{u},f)\in\mathcal{M}(\Omega)} \{\mathcal{L}(\boldsymbol{u}, f) := \mathcal{D}(\boldsymbol{u}) + \mathcal{S}(\boldsymbol{u}, f)\},
$$
$$
\text{s.t.} \quad \det\left(\nabla(\boldsymbol{\varphi} + \boldsymbol{u})\right) = f(\boldsymbol{x}), \quad \forall \boldsymbol{x} \in \Omega,
$$

(12)

where $\mathcal{S}(\boldsymbol{u}, f) = \frac{\tau_1}{2} \int_\Omega \|\nabla\boldsymbol{u}\|^2 d\boldsymbol{x} + \tau_2 \int_\Omega \phi(f)d\boldsymbol{x} + \frac{\tau_3}{2} \int_\Omega \|\nabla f\|^2 d\boldsymbol{x}$ is a combined regularizer and $\tau_3 > 0$ is a regulariztion parameter. The function space $[\mathcal{H}^1(\Omega)]^{d+1}$ is a reflexive Banach space, and its subset $\mathcal{M}(\Omega) \subset [\mathcal{H}^1(\Omega)]^{d+1}$ is convex.

3.2. Existence of minimizers and optimization

The penalty method is one of the most popular ways to recast an equality constraint optimization problem (12) to an unconstraint optimization problem [45], which is done by adding a penalty term to the objective functional that penalizes the violation of the constraints. Then, a quadratic penalty functional that penalizes the constraints of (12) in a Least-Squares (LS) sense is employed, leading to a modified bi-variant optimization problem which

is given as follow

$$\min_{\boldsymbol{\omega}\in\mathcal{M}(\Omega)} \left\{ \mathcal{L}_\lambda(\boldsymbol{\omega}) := \mathcal{L}_\lambda[\boldsymbol{u}, f] = \mathcal{D}(\boldsymbol{u}) + \mathcal{S}(\boldsymbol{u}, f) + \mathcal{C}(\boldsymbol{u}, f) \right\}, \tag{13}$$

where $\lambda > 0$ is a penalty parameter, and $C(\boldsymbol{\omega}) := C(\boldsymbol{u}, f) = \frac{\lambda}{2} \int_\Omega \left(\det \left(\nabla(\boldsymbol{\varphi} + \boldsymbol{u}) \right) - f(\boldsymbol{x}) \right)^2 d\boldsymbol{x}$. Especially if λ is chosen to be large enough, then the solution of (13) leads to an approximation solution that satisfies the equality constraint optimization (12).

Lemma 1. *Let Ω be an open bounded set of $\mathbb{R}^d$, and $(\boldsymbol{u}, f) \in \mathcal{M}(\Omega)$, then*

$$\|\boldsymbol{u}\|_{L^2(\Omega)} \le c_1 \|\nabla \boldsymbol{u}\|_{L^2(\Omega)}, \quad \|f - 1\|_{L^2(\Omega)} \le c_2 \|\nabla f\|_{L^2(\Omega)} \tag{14}$$

for some constants c_1 and c_2 depending only on d and Ω.

Proof 1. *Refer to [3, Poincaré inequality].*

In order to use the compactness results of [55] while still dealing with minimization problem (13), we obtain inequality property from Lemma 1 as follows:

$$\|\boldsymbol{\omega}\|_{\mathcal{M}(\Omega)} := \|\boldsymbol{u}\|_{L^2(\Omega)} + \|\nabla \boldsymbol{u}\|_{L^2(\Omega)} + \|f\|_{L^2(\Omega)} + \|\nabla f\|_{L^2(\Omega)} \le c_3 \mathcal{L}_\lambda[\boldsymbol{u}, f] + c_4, \tag{15}$$

for some constants c_3 and c_4 depending only on c_1, c_2, τ_1 and τ_3. Hence the coercive property of $\mathcal{L}_\lambda$ holds because

$$\mathcal{L}_\lambda(\boldsymbol{\omega}) \to +\infty \quad \text{as} \quad \|\boldsymbol{\omega}\|_{\mathcal{M}(\Omega)} \to \infty, \quad \boldsymbol{\omega} \in \mathcal{M}(\Omega). \tag{16}$$

The boundedness of $\mathcal{M}(\Omega)$ plays an important role in [55, Proposition 38.12]. Similarly, we also introduce this frequently used trick which reduces the minimum problem (13) on the unbounded set $\mathcal{M}(\Omega)$ of the Banach space $[\mathcal{H}^1(\Omega)]^{d+1}$ to an equivalent minimum problem

$$\min_{\boldsymbol{\omega}\in\mathcal{M}_{\boldsymbol{\omega}_0,r}(\Omega)} \mathcal{L}_\lambda(\boldsymbol{\omega}), \tag{17}$$

where $\mathcal{M}_{\boldsymbol{\omega}_0,r}(\Omega) := \mathcal{M}(\Omega) \cap \bar{U}\left(\boldsymbol{\omega}_0, r\right)$ and $\bar{U}\left(\boldsymbol{\omega}_0, r\right) \stackrel{\text{def}}{=} \left\{ \boldsymbol{\omega} \in [\mathcal{H}^1(\Omega)]^{d+1} : \|\boldsymbol{\omega} - \boldsymbol{\omega}_0\|_{\mathcal{M}(\Omega)} \le r \right\}$. Thus, $\mathcal{M}_{\boldsymbol{\omega}_0,r}(\Omega)$ is bounded.

Lemma 2. *For the functional $\mathcal{L}_\lambda(\boldsymbol{\omega}) : \mathcal{M}(\Omega) \subseteq [\mathcal{H}^1(\Omega)]^{d+1} \to [-\infty, \infty]$, where $\boldsymbol{\omega}_0 \in \mathcal{M}(\Omega)$, the minimum problem $\min_{\boldsymbol{\omega}\in\mathcal{M}(\Omega)} \mathcal{L}_\lambda(\boldsymbol{\omega})$ (i.e., the problem (13)) is equivalent to (17) when (16) holds and r is chosen sufficiently large.*

Proof 2. *Let $\mathcal{L}_\lambda(\boldsymbol{\omega}) \not\equiv +\infty$. By (16) there exists an $r > 0$ such that $\mathcal{L}_\lambda(\boldsymbol{\omega}) > \mathcal{L}_\lambda(\boldsymbol{\omega}_0)$ holds for all $\boldsymbol{\omega}$ with $\|\boldsymbol{\omega} - \boldsymbol{\omega}_0\|_{\mathcal{M}(\Omega)} > r$. Refer readers to [55, Corollary 38.14] for more details.*

To proceed, we make the following assumptions.

Assumption 1. *For any $x \in \Omega$, $\varphi \in C^{\ell+1}(\Omega)$ ($\ell \geq 0$) and $\omega \in \mathcal{M}(\Omega)$ (especially, $\omega \in \mathcal{M}_{\omega_0, r}(\Omega)$), there exists a constant $\mathcal{A}_0 > 0$, the following assumptions hold:*

1) *assume that two images $T(x)$ and $R(x)$ satisfy*

$$\max \left\{ \|T\|_{L^\infty(\Omega)}, \|R\|_{L^\infty(\Omega)}, \|\nabla T\|_{L^\infty(\Omega)}, \left\|\nabla^2 T\right\|_{L^\infty(\Omega)} \right\} < \mathcal{A}_0 < +\infty, \tag{18}$$

hence $\|T - R\|_{L^\infty(\Omega)} < 2\mathcal{A}_0$;

2) *assume that the positivity constraint function $\phi(f)$ is continuous when $f > 0$.*

Next, let us analyze the properties of the energy functional $\mathcal{L}_\lambda(\omega)$.

Lemma 3 (Lower semi-continuity of $S(\omega)$ and $C(\omega)$). *The bi-variant regularization functional $S(\omega) := S(u, f)$ in (17) and the penalty functional $C(\omega) := C(u, f)$ satisfy lower semi-continuity, i.e., let $\omega_j \in \mathcal{M}(\Omega)$ and $\omega_j \xrightarrow[L^1(\Omega)]{*} \omega$ ($j \to +\infty$); then*

$$S(\omega) \leq \lim_{j \to +\infty} S(\omega_j), \quad \text{and} \quad C(\omega) \leq \lim_{j \to +\infty} C(\omega_j). \tag{19}$$

Proof 3. *Define $S_1(\omega) := S_1(u, f) = \frac{\tau_1}{2} \int_\Omega \|\nabla u\|^2 dx + \frac{\tau_3}{2} \int_\Omega \|\nabla f\|^2 dx$. Since S_1 is convex, $epi(S_1) = \{(\omega, t) \in dom(S_1) \times \mathbb{R} : S_1(\omega) \leq t\}$ is convex. Hence, we can get that $epi(S_1)$ is weakly sequentially closed, which implies that S_1 is weakly sequentially lower semi-continuous (LSC). Combined with the continuity of $\phi(f)$ in Assumption 2), so $S(\omega)$ is weakly sequentially LSC.*

For any $x \in \Omega$, $\varphi \in C^{\ell+1}(\Omega)$ ($\ell \geq 0$) and $\omega \in \mathcal{M}(\Omega)$ (especially, $\omega \in \mathcal{M}_{\omega_0, r}(\Omega)$), there exists a constant $\mathcal{A}_1 > 0$, one has $\|(\nabla \bar{\varphi}_\theta)^*\|_{L^\infty(\Omega)} < \mathcal{A}_1 < +\infty$ and $c_5 = \|\det(\nabla \bar{\varphi}_\theta) - f\|_{L^\infty(\Omega)}$ is boundedness, hence the following inequality holds

$$|C(\omega) - C(\omega_0)| \leq \lambda c_5 \left(\int_\Omega |\langle (\nabla \bar{\varphi}_\theta)^*, \nabla(u - u_0) \rangle| dx + \int_\Omega |f - f_0| dx \right)$$
$$\leq c_6 \|\omega - \omega_0\|_{\mathcal{M}(\Omega)}, \tag{20}$$

where $\bar{\varphi}_\theta = \varphi + \theta u + (1 - \theta)u_0$ for any $\theta \in (0, 1)$, $c_6 = \lambda c_5 \cdot \max(\mathcal{A}_1, 1)$ and $(\nabla \bar{\varphi}_\theta)^*$ is the adjoint matrix of $\nabla \bar{\varphi}_\theta \in \mathbb{R}^{d \times d}$, which can also be seen from Lemma 6. The inequality (20) implies that the penalty functional $C(\omega) := C(u, f)$ satisfies lower semi-continuity.

Lemma 4 (Lower semi-continuity of $\mathcal{L}_\lambda$). *Assume that $T(x)$ is differentiable with respect to x. Then the functional $D(u)$ is lower semi-continuous, and consequently $\mathcal{L}_\lambda(\omega)$ from (17) is also LSC; i.e., for each $\epsilon > 0$ and $\omega = (u, f) \in \mathcal{M}(\Omega)$ with $D(u) < \infty$, there exists a $\delta_\epsilon > 0$ such that for all $\bar{\omega} = (\bar{u}, \bar{f}) \in \mathcal{M}(\Omega)$ satisfying $\|u - \bar{u}\|_{L^2(\Omega)} < \delta_\epsilon$, the inequality $D(u) < D(\bar{u}) + \epsilon$ holds.*

Proof 4. *Since the function $T(x)$ is differentiable, there exists a real number $\theta \in (0, 1)$ such that*

$$T(\varphi + u) = T(\varphi + \bar{u}) + \nabla T(s) \cdot h,$$

where $s = \varphi + \theta u + (1 - \theta)\bar{u}$ and $h = u - \bar{u}$. Hence we have

$$D(u) = D(\bar{u}) + \int_\Omega \left((T(\varphi + \bar{u}) - R(x))(\nabla T(s) \cdot h) + \frac{1}{2} h^T \left(\nabla T(s) \nabla T(s)^T \right) h \right) dx.$$

From (18), the above equation leads to

$$|D(u) - D(\bar{u})| \leq c_1 \|u - \bar{u}\|_{L^2(\Omega)} + c_2 \|u - \bar{u}\|_{L^2(\Omega)}^2, c_1 \geq 0, c_2 \geq 0.$$

In this case, we have, if taking $\delta(\epsilon) = \left(-c_1 + \sqrt{c_1^2 + 4\epsilon c_2}\right) / (2c_2)$, $\mathcal{D}(u) < \mathcal{D}(\bar{u}) + \epsilon$. Consequently, combined with Lemma 3, i.e., the lower semi-continuity of $S(\omega)$ and $C(\omega)$, the functional $\mathcal{L}_\lambda(\omega)$ from (17) is LSC. This proves the lemma.

The following Theorem illustrates that a more frequently used condition than Proposition 38.12. in [55] may be necessary to guarantee existence of minimizers of $\mathcal{L}_\lambda(\omega)$ over $\mathcal{M}(\Omega)$ in (13).

Theorem 1 (Existence). *A functional $\mathcal{L}_\lambda(\omega) : \mathcal{M}_{\omega_0,r}(\Omega) \subset [\mathcal{H}^1(\Omega)]^{d+1} \to [-\infty, \infty]$ on the convex, closed, and nonempty subset $\mathcal{M}_{\omega_0,r}(\Omega)$ of the real reflexive Banach space $[\mathcal{H}^1(\Omega)]^{d+1}$ satisfies (16), and is weak sequentially lower semi-continuous. Thus, the problem (17) possesses a minimum, in other words, the minimizatiom problem (13) admits a minimum.*

Proof 5. *Based on [55, Proposition 38.12(c)], the problem (17) has minimum because of the lower semi-continuity of $\mathcal{L}_\lambda$, the closed boundedness and convexity of $\mathcal{M}_{\omega_0,r}(\Omega)$ and reflexivity of the Banach space $[\mathcal{H}^1(\Omega)]^{d+1}$. From Lemma 2, we further show that the minimizatiom problem (13) admits a minimum.*

To deal with the stability of the solution scheme, we add a "proximal point" term into (13), leading to the iterative minimization problem defined by

$$\min_{(u,f)\in\mathcal{M}(\Omega)} \left\{ \mathcal{L}_\lambda^k[u, f; u^k] = \mathcal{D}(u) + \frac{\tau_1}{2}\int_\Omega \|\nabla u\|^2 dx + \tau_2 \int_\Omega \phi(f(x)) dx + \frac{\tau_3}{2}\int_\Omega |\nabla f(x)|^2 dx \right.$$
$$\left. + \frac{\lambda}{2}\int_\Omega \left(\det\left(\nabla(\varphi + u)\right) - f(x)\right)^2 dx + \frac{1}{2\gamma}\int_\Omega \|u - u^k\|^2 dx \right\}, \tag{21}$$

where $\gamma > 0$. Further, we split (21) into two subproblems as follows.

- The u-subproblem

$$u = \arg\min_{u\in\mathcal{V}} \left\{ \mathcal{D}(u) + \frac{\tau_1}{2}\int_\Omega \|\nabla u\|^2 dx \right.$$
$$\left. + \frac{\lambda}{2}\int_\Omega \left(\det\left(\nabla(\varphi + u)\right) - f(x)\right)^2 dx + \frac{1}{2\gamma}\int_\Omega \|u - u^k\|^2 dx \right\}. \tag{22}$$

- The f-subproblem

$$f = \arg\min_{f\in\mathcal{W}} \left\{ \tau_2 \int_\Omega \phi(f(x)) dx + \frac{\tau_3}{2}\int_\Omega |\nabla f(x)|^2 dx \right.$$
$$\left. + \frac{\lambda}{2}\int_\Omega \left(\det\left(\nabla(\varphi + u)\right) - f(x)\right)^2 dx \right\}. \tag{23}$$

Hence, the k-th update formulas of solving problem (21) are as follows

$$
\begin{cases}
\boldsymbol{u}^{k+1} = \arg\min_{\boldsymbol{u} \in \mathcal{V}} \left\{ \frac{1}{2} \int_{\Omega} \left(T(\boldsymbol{\varphi}^k + \boldsymbol{u}) - R \right)^2 d\boldsymbol{x} + \frac{\tau_1}{2} \int_{\Omega} \|\nabla \boldsymbol{u}\|^2 d\boldsymbol{x} \right. \\
\qquad\qquad \left. + \frac{\lambda^k}{2} \int_{\Omega} \left(\det\left(\nabla(\boldsymbol{\varphi}^k + \boldsymbol{u})\right) - f^k \right)^2 d\boldsymbol{x} + \frac{1}{2\gamma} \int_{\Omega} \|\boldsymbol{u} - \boldsymbol{u}^k\|^2 d\boldsymbol{x} \right\}, \\
f^{k+1} = \arg\min_{f \in \mathcal{W}} \left\{ \tau_2 \int_{\Omega} \phi(f) d\boldsymbol{x} + \frac{\tau_3}{2} \int_{\Omega} |\nabla f|^2 d\boldsymbol{x} \right. \\
\qquad\qquad \left. + \frac{\lambda^k}{2} \int_{\Omega} \left(\det\left(\nabla(\boldsymbol{\varphi}^k + \boldsymbol{u}^{k+1})\right) - f \right)^2 d\boldsymbol{x} \right\}, \\
\lambda^{k+1} = \rho \lambda^k, \quad \boldsymbol{\varphi}^{k+1} = \boldsymbol{\varphi}^k + \boldsymbol{u}^{k+1},
\end{cases}
\tag{24}
$$

where $\rho > 1$ is the growth factor of penalty parameter λ.

Next, we will derive the Gâteaux derivative of Jacobian determinant constraint in (24). Here we take the 2D case as an example, which can easily be extended to the 3D case. We first present three Lemmas as follows.

Lemma 5. *Let constant ϵ be small enough and vector $\boldsymbol{v} \in \mathcal{V}$ be a suitable perturbation of $\boldsymbol{u} \in \mathcal{V}$, assume that $\det(\nabla\boldsymbol{\varphi}) \neq 0$, then one has*

$$
\lim_{\epsilon \to 0} \frac{\det(\nabla\boldsymbol{\varphi} + \epsilon\nabla\boldsymbol{v}) - \det(\nabla\boldsymbol{\varphi})}{\epsilon} = \det(\nabla\boldsymbol{\varphi})\text{trace}\left(\nabla\boldsymbol{v}(\nabla\boldsymbol{\varphi})^{-1}\right) = \det(\nabla\boldsymbol{\varphi})(\nabla\boldsymbol{\varphi})^{-\top} \cdot \nabla\boldsymbol{v},
$$

where $A \cdot B$ denotes the matrix inner product $\sum_{i,j=1}^{2} A_{ij} B_{ij}$ between $A \in \mathbb{R}^{2\times2}$ and $B \in \mathbb{R}^{2\times2}$.

Proof 6. *Firstly, from the properties of determinant, we easily know*

$$
\begin{aligned}
\det(\nabla\boldsymbol{\varphi} + \epsilon\nabla\boldsymbol{v}) - \det(\nabla\boldsymbol{\varphi}) &= \det\left(\nabla\boldsymbol{\varphi} + \epsilon\nabla\boldsymbol{v}(\nabla\boldsymbol{\varphi})^{-1}\nabla\boldsymbol{\varphi}\right) - \det(\nabla\boldsymbol{\varphi}) \\
&= \left(\det\left(\boldsymbol{I}_d + \epsilon\nabla\boldsymbol{v}(\nabla\boldsymbol{\varphi})^{-1}\right) - 1\right)\det(\nabla\boldsymbol{\varphi}).
\end{aligned}
$$

Secondly, assume that $\nabla\boldsymbol{v}(\nabla\boldsymbol{\varphi})^{-1} =: \begin{pmatrix} a_{11} & a_{12} \\ a_{21} & a_{22} \end{pmatrix}$, we can deduce

$$
\begin{aligned}
\det\left(\boldsymbol{I}_d + \epsilon\nabla\boldsymbol{v}(\nabla\boldsymbol{\varphi})^{-1}\right) - 1 &= \begin{vmatrix} 1 + \epsilon a_{11} & \epsilon a_{12} \\ \epsilon a_{21} & 1 + \epsilon a_{22} \end{vmatrix} - 1 \\
&= \epsilon a_{11} + \epsilon a_{22} + \epsilon^2 a_{11} a_{22} - \epsilon^2 a_{12} a_{21},
\end{aligned}
\tag{25}
$$

then it is easy to check that

$$
\lim_{\epsilon \to 0} \frac{\det\left(\boldsymbol{I}_d + \epsilon\nabla\boldsymbol{v}(\nabla\boldsymbol{\varphi})^{-1}\right) - 1}{\epsilon} = a_{11} + a_{22} = trace(\nabla\boldsymbol{v}(\nabla\boldsymbol{\varphi})^{-1}),
$$

hence we obtain

$$
\lim_{\epsilon \to 0} \frac{\det(\nabla\boldsymbol{\varphi} + \epsilon\nabla\boldsymbol{v}) - \det(\nabla\boldsymbol{\varphi})}{\epsilon} = \det(\nabla\boldsymbol{\varphi})trace\left(\nabla\boldsymbol{v}(\nabla\boldsymbol{\varphi})^{-1}\right).
\tag{26}
$$

Finally, assume that $\nabla\boldsymbol{v} := \begin{pmatrix} v_{11} & v_{12} \\ v_{21} & v_{22} \end{pmatrix}$ and $(\nabla\boldsymbol{\varphi})^{-1} := \begin{pmatrix} b_{11} & b_{12} \\ b_{21} & b_{22} \end{pmatrix}$, we have

$$
trace\left(\nabla\boldsymbol{v}(\nabla\boldsymbol{\varphi})^{-1}\right) = v_{11}b_{11} + v_{12}b_{21} + v_{21}b_{12} + v_{22}b_{22}
$$

and

$$(\nabla\boldsymbol{\varphi})^{-\top} \cdot \nabla\boldsymbol{v} = \begin{pmatrix} b_{11} & b_{21} \\ b_{12} & b_{22} \end{pmatrix} \cdot \begin{pmatrix} v_{11} & v_{12} \\ v_{21} & v_{22} \end{pmatrix} = v_{11}b_{11} + v_{12}b_{21} + v_{21}b_{12} + v_{22}b_{22}.$$

Therefore, we can deduce that

$$trace\big(\nabla\boldsymbol{v}(\nabla\boldsymbol{\varphi})^{-1}\big) = (\nabla\boldsymbol{\varphi})^{-\top} \cdot \nabla\boldsymbol{v}, \tag{27}$$

which shows the assertion.

Lemma 6. *Let $\boldsymbol{v} \in \mathcal{V}$ be an arbitrary perturbation of $\boldsymbol{u}$. Thus, the Gâteaux derivative of $C(\boldsymbol{u}) := \int_{\Omega}(\det(\nabla(\boldsymbol{\varphi} + \boldsymbol{u})) - f)^2 d\boldsymbol{x}$ is given by*

$$\frac{\partial C(\boldsymbol{u})}{\partial \boldsymbol{u}}\boldsymbol{v} = \int_{\Omega} \langle -2\nabla \cdot \mathcal{U}(\boldsymbol{u})(\boldsymbol{x}), \boldsymbol{v}\rangle\, d\boldsymbol{x},$$

where $\mathcal{U}(\boldsymbol{u})(\boldsymbol{x}) := \det(\nabla(\boldsymbol{\varphi} + \boldsymbol{u}))(\nabla(\boldsymbol{\varphi} + \boldsymbol{u}))^{-\top}(\det(\nabla(\boldsymbol{\varphi} + \boldsymbol{u})) - f).$

Proof 7. *For any $\boldsymbol{u}, \boldsymbol{v} \in \mathcal{V}$, let us define outer normal vector $\boldsymbol{n}$ on boundary $\partial\Omega$ and any small enough constant ϵ, from (26) and (27) in Lemma 5 one has*

$$\int_{\partial\Omega} \left\langle \frac{\partial \mathcal{U}(\boldsymbol{u})(\boldsymbol{x})}{\partial \boldsymbol{n}}, \boldsymbol{v} \right\rangle d\boldsymbol{s} = 0,$$

and

$$
\begin{aligned}
\frac{\partial C(\boldsymbol{u})}{\partial \boldsymbol{u}}\boldsymbol{v} &= \lim_{\epsilon \to 0} \frac{C[\boldsymbol{u} + \epsilon\boldsymbol{v}] - C(\boldsymbol{u})}{\epsilon} \\
&= \lim_{\epsilon \to 0} \int_{\Omega} \frac{[\det(\nabla(\boldsymbol{\varphi} + \boldsymbol{u}) + \epsilon\nabla\boldsymbol{v}) - \det(\nabla(\boldsymbol{\varphi} + \boldsymbol{u}))]}{\epsilon} \\
&\qquad\qquad\qquad \cdot [\det(\nabla(\boldsymbol{\varphi} + \boldsymbol{u}) + \epsilon\nabla\boldsymbol{v}) + \det(\nabla(\boldsymbol{\varphi} + \boldsymbol{u})) - 2f]d\boldsymbol{x} \\
&\overset{(26)}{=\!=\!=} \int_{\Omega} [\det(\nabla(\boldsymbol{\varphi} + \boldsymbol{u})) \cdot trace(\nabla\boldsymbol{v}(\nabla(\boldsymbol{\varphi} + \boldsymbol{u}))^{-1})][2\det(\nabla(\boldsymbol{\varphi} + \boldsymbol{u})) - 2f]d\boldsymbol{x} \\
&\overset{(27)}{=\!=\!=} \int_{\Omega} 2\left\langle \det(\nabla(\boldsymbol{\varphi} + \boldsymbol{u}))(\nabla(\boldsymbol{\varphi} + \boldsymbol{u}))^{-\top}(\det(\nabla(\boldsymbol{\varphi} + \boldsymbol{u})) - f), \nabla\boldsymbol{v} \right\rangle d\boldsymbol{x} \\
&= \int_{\Omega} 2\langle \mathcal{U}(\boldsymbol{u})(\boldsymbol{x}), \nabla\boldsymbol{v}\rangle d\boldsymbol{x} - \int_{\partial\Omega} 2\left\langle \frac{\partial \mathcal{U}(\boldsymbol{u})(\boldsymbol{x})}{\partial \boldsymbol{n}}, \boldsymbol{v} \right\rangle d\boldsymbol{s} \\
&= \int_{\Omega} \langle -2\nabla \cdot \mathcal{U}(\boldsymbol{u})(\boldsymbol{x}), \boldsymbol{v}\rangle d\boldsymbol{x},
\end{aligned}
$$

which proves the assertion.

Lemma 7. *Let $\boldsymbol{u} \in \mathcal{V}$ be a suitable perturbation of $\boldsymbol{\varphi}$, then one has*

$$
\begin{aligned}
\nabla \cdot \Big[\det(\nabla(\boldsymbol{\varphi} + \boldsymbol{u}))&(\nabla(\boldsymbol{\varphi} + \boldsymbol{u}))^{-\top}\big(\det(\nabla(\boldsymbol{\varphi} + \boldsymbol{u})) - f\big)\Big] \\
&= \det(\nabla(\boldsymbol{\varphi} + \boldsymbol{u}))(\nabla(\boldsymbol{\varphi} + \boldsymbol{u}))^{-\top}\nabla\big(\det(\nabla(\boldsymbol{\varphi} + \boldsymbol{u})) - f\big).
\end{aligned}
$$

Proof 8. *Since we have the inclusion from the property of the determinant*

$$\det(\nabla(\boldsymbol{\varphi} + \boldsymbol{u}))(\nabla(\boldsymbol{\varphi} + \boldsymbol{u}))^{-\top} = (\nabla(\boldsymbol{\varphi} + \boldsymbol{u}))^{*\top} := \begin{pmatrix} (\varphi^2 + u^2)_{x_2} & -(\varphi^2 + u^2)_{x_1} \\ -(\varphi^1 + u^1)_{x_2} & (\varphi^1 + u^1)_{x_1} \end{pmatrix}, \tag{28}$$

so it is easy to obtain

$$\nabla \cdot \Big[\det(\nabla(\boldsymbol{\varphi} + \boldsymbol{u}))(\nabla(\boldsymbol{\varphi} + \boldsymbol{u}))^{-\top}\Big] = \boldsymbol{0}. \tag{29}$$

In particular, the formula (29) *is also true for the 3D case. Finally, we simplify*

$$\nabla \cdot \left[\det(\nabla(\boldsymbol{\varphi} + \boldsymbol{u}))(\nabla(\boldsymbol{\varphi} + \boldsymbol{u}))^{-\top} \left(\det(\nabla(\boldsymbol{\varphi} + \boldsymbol{u})) - f \right) \right]$$
$$= \left(\det(\nabla(\boldsymbol{\varphi} + \boldsymbol{u})) - f \right) \nabla \cdot \left[\det(\nabla(\boldsymbol{\varphi} + \boldsymbol{u}))(\nabla(\boldsymbol{\varphi} + \boldsymbol{u}))^{-\top} \right]$$
$$+ \det(\nabla(\boldsymbol{\varphi} + \boldsymbol{u}))(\nabla(\boldsymbol{\varphi} + \boldsymbol{u}))^{-\top} \nabla \left(\det(\nabla(\boldsymbol{\varphi} + \boldsymbol{u})) - f \right)$$
$$= \det(\nabla(\boldsymbol{\varphi} + \boldsymbol{u}))(\nabla(\boldsymbol{\varphi} + \boldsymbol{u}))^{-\top} \nabla \left(\det(\nabla(\boldsymbol{\varphi} + \boldsymbol{u})) - f \right),$$

which proves the assertion.

To obtain the optimal solution of the $\boldsymbol{u}$-subproblem, we consider its Euler–Lagrange equation, which is equivalent to solving

$$\left(T(\boldsymbol{\varphi}^k + \boldsymbol{u}) - R \right) \nabla T - \tau_1 \Delta \boldsymbol{u} + \frac{1}{\gamma}(\boldsymbol{u} - \boldsymbol{u}^k)$$
$$- \lambda^k \det \left(\nabla(\boldsymbol{\varphi}^k + \boldsymbol{u}) \right) \left(\nabla(\boldsymbol{\varphi}^k + \boldsymbol{u}) \right)^{-\top} \nabla \left[\det \left(\nabla(\boldsymbol{\varphi}^k + \boldsymbol{u}) \right) - f^k \right] = \boldsymbol{0}. \tag{30}$$

The above nonlinear systems (30) with the boundary condition $\boldsymbol{u} = \boldsymbol{0}$ can be written as

$$\begin{cases} -\tau_1 \Delta \boldsymbol{u} + \frac{1}{\gamma}\boldsymbol{u} &= \boldsymbol{r}(\boldsymbol{u}), \quad \text{in } \Omega, \\ \boldsymbol{u} &= \boldsymbol{0}, \quad\quad \text{on } \partial\Omega, \end{cases} \tag{31}$$

where $\boldsymbol{r}(\boldsymbol{u}) = -\left(T(\boldsymbol{\varphi}^k + \boldsymbol{u}) - R \right) \nabla T + \lambda^k \det \left(\nabla(\boldsymbol{\varphi}^k + \boldsymbol{u}) \right) \left(\nabla(\boldsymbol{\varphi}^k + \boldsymbol{u}) \right)^{-\top} \nabla \left[\det \left(\nabla(\boldsymbol{\varphi}^k + \boldsymbol{u}) \right) - f^k \right] + \frac{1}{\gamma}\boldsymbol{u}^k$. The nonlinear partial differential equations (31) are difficult to be directly solved, here a simple linearization technique is used, leading to the systems as follows

$$\begin{cases} -\tau_1 \Delta \boldsymbol{u} + \frac{1}{\gamma}\boldsymbol{u} &= \boldsymbol{r}(\boldsymbol{u}^k), \quad \text{in } \Omega, \\ \boldsymbol{u} &= \boldsymbol{0}, \quad\quad \text{on } \partial\Omega. \end{cases} \tag{32}$$

Once the solution $\boldsymbol{u}^{k+1}$ of (32) is obtained, we minimize the f-subproblem by fixing $\boldsymbol{u}^{k+1}$. In other words, we look for $f^{k+1}(\boldsymbol{x})$ by solving the Euler–Lagrange equation

$$\tau_2 d\phi(f) - \tau_3 \Delta f - \lambda \left(\det \left(\nabla(\boldsymbol{\varphi}^k + \boldsymbol{u}^{k+1}) \right) - f \right) = 0, \tag{33}$$

where $d\phi(f) := d\phi_1(f) = 1 - 1/f^2$ and $d\phi(f) := d\phi_2(f) = \log(f) + 1 - 1/f$ for the functions $\phi_1(f)$ and $\phi_2(f)$, respectively. Combined with the boundary condition $f(\boldsymbol{x}) = 1$ on $\partial\Omega$, the optimal solution of the

f-subproblem can be seen as the solution of the system defined by

$$
\begin{cases}
-\tau_3 \Delta f + \lambda f & = \lambda \det\left(\nabla(\boldsymbol{\varphi}^k + \boldsymbol{u}^{k+1}))\right) - \tau_2 d\phi(f^k), & \text{in } \Omega, \\
f & = 1, & \text{on } \partial\Omega.
\end{cases}
\tag{34}
$$

Remark 1. *As described above, our model can theoretically ensure that $f(\boldsymbol{x}) > 0$. However, $f(\boldsymbol{x})$ may not be almost positive everywhere due to the multiple modeling parameter choices and not better handling the nonlinear part of* (34). *To avoid grid folding, we adopt the deformation correction technique in numerical implementation* (refer *to Section 4.1.2 for more details*).

4. Numerical implementation

Before we describe the numerical algorithm for solving the proposed model, we first briefly introduce the discretization of the systems (32) and (34). Without loss of generality, we focus on the discretization of two-dimensional space. Such a discretization technique is easily extended to three-dimensional space.

4.1. Discretization

In this part, we exploit the optimize-discretize method to solve the diffeomorphic model (13). Here, a uniform Cartesian grid of $m \times n$ is constructed on the image domain $\Omega := [0,1]^2$. We assume that each pixel is a box of lengths $h_x = 1/m$ and $h_y = 1/n$, identifying pixels with cell-centered grid points. Thus the discrete image domain is denoted by $\Omega_h = \{(x_i, y_j) \mid x_i = (i - 1/2)h_x, y_j = (j - 1/2)h_y, i = 1, \cdots, m, \ j = 1, \cdots, n\}$, and (i, j) denotes the index of the coordinate (x_i, y_j).

Typically, the finite difference scheme is used to approximate the first- and second-order derivatives in image processing. We denote the discrete schemes applied to functions $v \in \mathbb{R}$ and $\boldsymbol{u} = (u^1, u^2)^\top \in \mathbb{R}^2$ at the grid point (i, j) by

$$
(\nabla v)_{i,j} = (\delta_x v_{i,j}, \delta_y v_{i,j})^\top, \quad (\nabla \cdot \boldsymbol{u})_{i,j} = \delta_x u^1_{i,j} + \delta_y u^2_{i,j},
$$
$$
(\Delta u^\ell)_{i,j} = \delta_{xx} u^\ell_{i,j} + \delta_{yy} u^\ell_{i,j}, \quad (\Delta \boldsymbol{u})_{i,j} = \left((\Delta u^1)_{i,j}, (\Delta u^2)_{i,j}\right)^\top,
$$

where $\ell = 1$ or 2, and

$$
\delta_x v_{i,j} = (v_{i+1,j} - v_{i-1,j})/(2h_x), \qquad \delta_y v_{i,j} = (v_{i,j+1} - v_{i,j-1})/(2h_y),
$$
$$
\delta_{xx} u^\ell_{i,j} = (u^\ell_{i-1,j} - 2u^\ell_{i,j} + u^\ell_{i+1,j})/h_x^2, \quad \delta_{yy} u^\ell_{i,j} = (u^\ell_{i,j-1} - 2u^\ell_{i,j} + u^\ell_{i,j+1})/h_y^2.
$$

4.1.1. The discrete forms of two subproblems

To proceed, let us define $C = \det\left(\nabla(\boldsymbol{\varphi} + \boldsymbol{u})\right) - f$. Based on the above definitions, the finite difference approximation $C_{i,j}^k$ of C at the grid point (i,j) can be denoted as

$$
\begin{aligned}
C_{i,j}^k &:= \left[\det\left(\nabla(\boldsymbol{\varphi}^k + \boldsymbol{u}^k)\right) - f^k\right]\bigg|_{i,j} = \begin{vmatrix} \delta_x(\varphi_{i,j}^{1,k} + u_{i,j}^{1,k}) & \delta_y(\varphi_{i,j}^{1,k} + u_{i,j}^{1,k}) \\ \delta_x(\varphi_{i,j}^{2,k} + u_{i,j}^{2,k}) & \delta_y(\varphi_{i,j}^{2,k} + u_{i,j}^{2,k}) \end{vmatrix} - f_{i,j}^k \\
&= (\delta_x\varphi_{i,j}^{1,k} + \delta_x u_{i,j}^{1,k})(\delta_y\varphi_{i,j}^{2,k} + \delta_y u_{i,j}^{2,k}) - (\delta_y\varphi_{i,j}^{1,k} + \delta_y u_{i,j}^{1,k})(\delta_x\varphi_{i,j}^{2,k} + \delta_x u_{i,j}^{2,k}) - f_{i,j}^k.
\end{aligned}
$$

See also Section 4.1.2 for more details. From Equation (28), it is easy to obtain

$$
\begin{aligned}
&\det\left(\nabla(\boldsymbol{\varphi} + \boldsymbol{u})\right)\left(\nabla(\boldsymbol{\varphi} + \boldsymbol{u})\right)^{-\mathsf{T}}\nabla C \\
&= \begin{pmatrix} \delta_y(\varphi^2 + u^2) & -\delta_x(\varphi^2 + u^2) \\ -\delta_y(\varphi^1 + u^1) & \delta_x(\varphi^1 + u^1) \end{pmatrix}(\delta_x C, \delta_y C)^{\mathsf{T}} \\
&= \left(\delta_x C \cdot \delta_y(\varphi^2 + u^2) - \delta_y C \cdot \delta_x(\varphi^2 + u^2), -\delta_x C \cdot \delta_y(\varphi^1 + u^1) + \delta_y C \cdot \delta_x(\varphi^1 + u^1)\right)^{\mathsf{T}},
\end{aligned}
$$

hence the finite difference approximation of the $\boldsymbol{u}$-subproblem (32) is given by

$$
\begin{cases}
-\tau_1(\delta_{xx} + \delta_{yy} + \dfrac{1}{\tau_1\gamma})u_{i,j}^{1,k+1} = -(T^k - R)_{i,j}\delta_x T_{i,j}^k + \dfrac{1}{\gamma}u_{i,j}^{1,k} \\
\qquad\qquad +\lambda^k\left[(\delta_y\varphi_{i,j}^{2,k} + \delta_y u_{i,j}^{2,k})\delta_x C_{i,j}^k - (\delta_x\varphi_{i,j}^{2,k} + \delta_x u_{i,j}^{2,k})\delta_y C_{i,j}^k\right], \\
-\tau_1(\delta_{xx} + \delta_{yy} + \dfrac{1}{\tau_1\gamma})u_{i,j}^{2,k+1} = -(T^k - R)_{i,j}\delta_y T_{i,j}^k + \dfrac{1}{\gamma}u_{i,j}^{2,k} \\
\qquad\qquad -\lambda^k\left[(\delta_y\varphi_{i,j}^{1,k} + \delta_y u_{i,j}^{1,k})\delta_x C_{i,j}^k - (\delta_x\varphi_{i,j}^{1,k} + \delta_x u_{i,j}^{1,k})\delta_y C_{i,j}^k\right],
\end{cases} \tag{35}
$$

where $T^k := T(\boldsymbol{\varphi}^k + \boldsymbol{u}^k)$ and the finite difference approximation of the f-subproblem (34) is given by

$$
\begin{aligned}
-\tau_3(\delta_{xx} + \delta_{yy})f_{i,j}^{k+1} + \lambda^k f_{i,j}^{k+1} &= \lambda^k\left(\delta_x\varphi_{i,j}^{1,k} + \delta_x u_{i,j}^{1,k}\right)(\delta_y\varphi_{i,j}^{2,k} + \delta_y u_{i,j}^{2,k}) \\
&\quad - \lambda^k(\delta_y\varphi_{i,j}^{1,k} + \delta_y u_{i,j}^{1,k})(\delta_x\varphi_{i,j}^{2,k} + \delta_x u_{i,j}^{2,k}) - \tau_2 d\phi(f_{i,j}^k),
\end{aligned} \tag{36}
$$

where $d\phi_1(f_{i,j}^k) = 1 - \dfrac{1}{(f_{i,j}^k)^2}$ or $d\phi_2(f_{i,j}^k) = \log(f_{i,j}^k) + 1 - \dfrac{1}{f_{i,j}^k}$.

4.1.2. Discretizing the Jacobian determinant

Similar to our previous work [60], the Jacobian determinant $\det(\nabla\boldsymbol{\varphi})|_o$ of the deformation $o := \varphi_{i,j}$ at the cell center (i,j) (*see* Figure 1) is given by

$$
\det(\nabla\boldsymbol{\varphi})|_o = \begin{vmatrix} \delta_x\varphi_{i,j}^1 & \delta_y\varphi_{i,j}^1 \\ \delta_x\varphi_{i,j}^2 & \delta_y\varphi_{i,j}^2 \end{vmatrix} = \frac{1}{4h_x h_y}\begin{vmatrix} \varphi_{i+1,j}^1 - \varphi_{i-1,j}^1 & \varphi_{i,j+1}^1 - \varphi_{i,j-1}^1 \\ \varphi_{i+1,j}^2 - \varphi_{i-1,j}^2 & \varphi_{i,j+1}^2 - \varphi_{i,j-1}^2 \end{vmatrix}
$$

$$= \frac{1}{4h_x h_y} \left(\left| \begin{array}{cc} \varphi^1_{i+1,j} - \varphi^1_{i,j} & \varphi^1_{i,j+1} - \varphi^1_{i,j} \\ \varphi^2_{i+1,j} - \varphi^2_{i,j} & \varphi^2_{i,j+1} - \varphi^2_{i,j} \end{array} \right| + \left| \begin{array}{cc} \varphi^1_{i,j+1} - \varphi^1_{i,j} & \varphi^1_{i-1,j} - \varphi^1_{i,j} \\ \varphi^2_{i,j+1} - \varphi^2_{i,j} & \varphi^2_{i-1,j} - \varphi^2_{i,j} \end{array} \right| \right.$$

$$\left. + \left| \begin{array}{cc} \varphi^1_{i-1,j} - \varphi^1_{i,j} & \varphi^1_{i,j-1} - \varphi^1_{i,j} \\ \varphi^2_{i-1,j} - \varphi^2_{i,j} & \varphi^2_{i,j-1} - \varphi^2_{i,j} \end{array} \right| + \left| \begin{array}{cc} \varphi^1_{i,j-1} - \varphi^1_{i,j} & \varphi^1_{i+1,j} - \varphi^1_{i,j} \\ \varphi^2_{i,j-1} - \varphi^2_{i,j} & \varphi^2_{i+1,j} - \varphi^2_{i,j} \end{array} \right| \right)$$

$$= \frac{1}{2} \left(R^{i,j}_{\Delta obd} + R^{i,j}_{\Delta oda} + R^{i,j}_{\Delta oac} + R^{i,j}_{\Delta ocb} \right),$$

where $R^{i,j}_{\Delta obd}$ is an area ratio of the triangle signed area

$$\frac{1}{2} \left| \begin{array}{cc} \varphi^1_{i+1,j} - \varphi^1_{i,j} & \varphi^1_{i,j+1} - \varphi^1_{i,j} \\ \varphi^2_{i+1,j} - \varphi^2_{i,j} & \varphi^2_{i,j+1} - \varphi^2_{i,j} \end{array} \right|$$

to the area element $h_x h_y$.

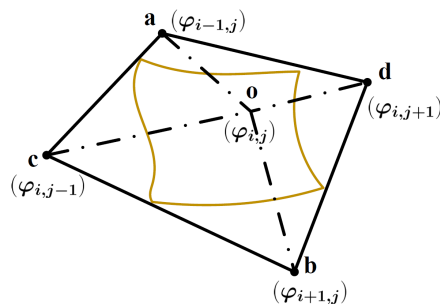**Figure 1:** Finite difference computation involved the Jacobian determinant $\det(\nabla \varphi)|_o$ of the deformation $o := \varphi_{i,j}$ at the cell center (i, j) for $d = 2$.

In particular, if one of the ratios $R^{i,j}_\Delta$ is negative and the others are positive, the Jacobian determinant $\det(\nabla \varphi)|_o$ may also be positive although a twist has occurred. At this time, box-based area measures do not detect twists. To prevent twists and singular points, we propose a signed area minimum ratio indicator $R_{i,j}$ that can detect twists of the grid

$$R_{i,j} = \min \left\{ R^{i,j}_{\Delta obd}, R^{i,j}_{\Delta oda}, R^{i,j}_{\Delta oac}, R^{i,j}_{\Delta ocb} \right\}. \tag{37}$$

Once $R_{i,j}$ is negative, we will exploit the deformation correction strategy to correct the triangles with negative area ratios. Firstly, we collect the grid folding points, such as points g, o and b in Figure 2(a). Then we choose a folding key point with a large folding degree, where the folding degree $\text{Deg}(p)$ is defined as the number of edges containing point p in a triangle with a negative area ratio. For example, point b is a folding key point due to $\text{Deg}(b) = 5, \text{Deg}(g) = \text{Deg}(o) = 3$ in Figure 2(a). Finally, we move point b to b' to ensure that the grid unfolding
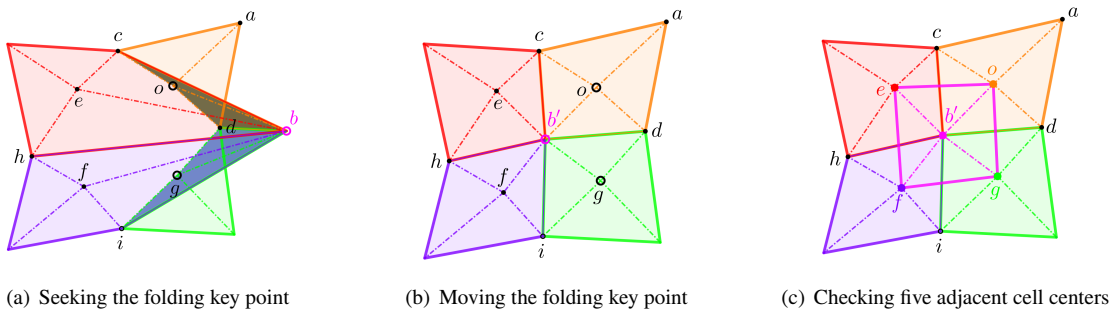
(a) Seeking the folding key point (b) Moving the folding key point (c) Checking five adjacent cell centers

Figure 2: Grid folding correction.

indicators of the five adjacent center points (e, f, g, o and b' respectively) are all positive, *see* Figure 2(b) and Figure 2(c). The corresponding grid correction strategy has been presented in the Algorithm 1. Obviously, this approach can be easily extended to 3D, *see* [60] for more details.

Algorithm 1 Deformation correction

Input: $\boldsymbol{\varphi}$;
1 Initialization: $\epsilon = 10^{-2}$;
2 Compute $\{R_1, R_2, R_3, R_4\} := \{R_{\triangle obd}, R_{\triangle oda}, R_{\triangle oac}, R_{\triangle ocb}\}$ and
  $R_{i,j} := \min \{R_1(i,j), R_2(i,j), R_3(i,j), R_4(i,j)\}$;
3 Find $S := \{(i,j) \mid R_{i,j} < \epsilon\}$ and the folding points set P causing the overlaps
  $P := \{P_{i,j} \in \{(i,j), (i-1,j), (i,j-1), (i+1,j), (i,j+1) \mid (i,j) \in S\}\}$;
4 **if** $P = \varnothing$ **then**
5 | Exit this algorithm;
6 **else**
7 | **foreach** $(i,j) \in P$ **do**
8 | Optimize $\boldsymbol{\varphi}_{i,j}$ such that $\min\{R_{i,j}, R_{i-1,j}, R_{i,j-1}, R_{i+1,j}, R_{i,j+1}\} \geq \epsilon$;
9 | **end**
10 **end**
11 $R_{min} = \min\{R_{i,j}\}$;
Output: $\boldsymbol{\varphi}, R_{min}$.

4.2. Numerical algorithms

In general due to the nonconvexity of the optimization problem (12), seeking global minimum of the displacement field $\boldsymbol{u}$-subproblem is difficult and computationally challenging. Here, we first introduce the algorithm based on the penalty algorithm, which solves the proposed diffeomorphic registration model with the deformed Jacobian equation constraint where $f(\boldsymbol{x})$ is an unknown optimized variant. Then, we extend our paradigm to address multilevel registration between two arbitrary volumes on liver CT scans, called image-to-image registration.

Firstly, the diffeomorphic image registration algorithm that employs the penalty method and combines with the deformation correction technique is designed. The detailed steps of solving the diffeomorphic registration model with Jacobian determinant constraint are summarized in Algorithm 2.

Algorithm 2 Diffeomorphic image registration based on penalty method (DIRPM)

Input: $R, T, \boldsymbol{\varphi}^1, f^1, \tau_1, \tau_2, \tau_3, \lambda^1, \gamma, \rho, MaxIter$;

1 Initialization: $\boldsymbol{u}^1 = \boldsymbol{0}, \epsilon_{\mathcal{L}} = 10^{-3}, \epsilon_u = 10^{-2}$;

2 **for** $k = 1, \cdots, MaxIter$ **do**

3   Determine displacement field $\boldsymbol{u}^{k+1}$ by solving the equation (32);

4   Update deformation field $\boldsymbol{\varphi}^{k+1} = \boldsymbol{\varphi}^k + \boldsymbol{u}^{k+1}$;

5   Correct $\boldsymbol{\varphi}^{k+1}$ and obtain grid unfolding indicator R_{min}^{k+1} by Algorithm 1;

6   Determine f^{k+1} by solving the equation (34);

7   Update the penalty factor $\lambda^{k+1} = \rho \lambda^k$;

8   **if** $\frac{\|\mathcal{L}_\lambda^k(\boldsymbol{u}^{k+1}, f^k; \boldsymbol{u}^k) - \mathcal{L}_\lambda^k(\boldsymbol{u}^k, f^k; \boldsymbol{u}^k)\|}{\|\mathcal{L}_\lambda^1(\boldsymbol{u}^1, f^1; \boldsymbol{u}^1)\|} \leq \epsilon_{\mathcal{L}}$ or $\frac{\|\boldsymbol{u}^{k+1} - \boldsymbol{u}^k\|}{\|\boldsymbol{u}^1\|} \leq \epsilon_u$ **then** break; ;

9 **end**

10 $T^{new} = T(\boldsymbol{\varphi}^{k+1})$;

11 $\boldsymbol{\varphi}^{new} = \boldsymbol{\varphi}^{k+1}$;

12 $f^{new} = f^{k+1}$;

Output: $T^{new}, \boldsymbol{\varphi}^{new}, f^{new}$.

Secondly, since the proposed model is non-convex and highly non-linear, then a solving algorithm based on the multilevel strategy, which is a standard approach used to avoid getting trapped in a meaningless local minimum, is proposed for the optimization to reduce the overall computational cost of the solution scheme. We hierarchically decompose the original finest level registration problem into different coarsened multilevel subproblems which are then fast and easier to be solved than the original one. Its general idea is to provide an initial approximation on a finer grid by the interpolation of approximated solutions on coarser grids. In fact, this principle simply means that a coarser discretization level is used to provide a good initial approximation for the iteration on the next finer discretization level [49]. The multilevel scheme is summarized in Algorithm 3.

Algorithm 3 Multilevel Registration

Input: $R, T, L, \tau_1, \tau_2, \tau_3, \lambda, \gamma, \rho, MaxIter$;

1 Initialization: $R_1 = R, T_1 = T, \boldsymbol{\varphi}_L = \boldsymbol{x}, f_L = 1$;

2 **for** $\ell = 2, \cdots, L$ **do**

3   Compute the *reference* and *template* images for the ℓ-level coarse grid:
        $R_\ell = I_h^H R_{\ell-1}, T_\ell = I_h^H T_{\ell-1}$;

4 **end**

5 **for** $\ell = L, \cdots, 1$ **do**

6   Call the diffeomorphic image registration Algorithm 2 based on penalty method:

7      $[T_\ell^{new}, \boldsymbol{\varphi}_\ell^{new}, f_\ell^{new}] = \text{DIRPM}(R_\ell, T_\ell, \boldsymbol{\varphi}_\ell, f_\ell, \tau_1, \tau_2, \tau_3, \lambda, \gamma, \rho, MaxIter)$;

8   **if** $\ell > 1$ **then** Interpolation (or prolongation): $\boldsymbol{\varphi}_{\ell-1} = I_H^h \boldsymbol{\varphi}_\ell^{new}, f_{\ell-1} = I_H^h f_\ell^{new}$;

9 **end**

Output: $T_1^{new}, \boldsymbol{\varphi}_1^{new}$.

---

5. Numerical experiments

To evaluate the performance of the proposed method and the other popular methods for 2D and 3D images, we will show visualizations of registration results as qualitative evaluations, such as the registered images, the

---

errors between the registered image $T(\bar{\varphi}(x))$ and $R(x)$, the deformation grids, the displacement fields, and the Jacobian determinant hotmaps of the deformation fields. Besides, we also provide quantitative assessments using the popular metrics, including

i.) the grid unfolding indicator $R_{\min}$ and the grid folding ratio (GFR) which are defined by

$$R_{\min} = \min_{i,j} R_{i,j}, \quad \text{and} \quad \text{GFR} = \frac{\sharp(\mathcal{D})}{\sharp(\Omega_h)},$$

where $\sharp(\mathcal{D})$ and $\sharp(\Omega_h)$ denote the numbers of nodes in $\mathcal{D}$ and Ω_h, respectively.

ii.) the Jacobian determinant measures are defined by

$$\det(\nabla\bar{\varphi})|_{i,j}, \qquad \overline{\det}(J(\bar{\varphi})) = \frac{1}{mn} \sum_{i,j} \det(\nabla\bar{\varphi})|_{i,j},$$

$$\det_{\min}(J(\bar{\varphi})) = \min_{i,j} \det(\nabla\bar{\varphi})|_{i,j}, \qquad \det_{\max}(J(\bar{\varphi})) = \max_{i,j} \det(\nabla\bar{\varphi})|_{i,j}.$$

iii.) the relative sum of squared differences (Re_SSD), which is defined by

$$\text{Re\_SSD}(T, R, T(\bar{\varphi})) = \frac{\sum_{i,j}(T(\bar{\varphi}_{i,j}) - R_{i,j})^2}{\sum_{i,j}(T_{i,j} - R_{i,j})^2}.$$

iv.) the *ssim* and *psnr* metrics are widely used to describe the degree of structure distortion and pixel blurring, respectively. We use them here for comparing the registered images with the other popular methods. In general, the registration results are better if their *ssim* and *psnr* values are higher.

5.1. Comparisons of different penalty functions

In this part, two examples are implemented to investigate how sensitive the proposed registration model (11) is with respect to different control functions ϕ_1 and ϕ_2. In local large deformation image registration problems, the uniform Jacobian determinant constraint leads that the transformation between the template and the reference may not be optimal: if the value $\det(\nabla\bar{\varphi}) = 1$ is fixed at each pixel, then the corresponding deformation field $\bar{\varphi}(x)$ is pointwise volume-preserving, but it may be a poor transformation for local matching between reference and template images. Alternatively, the relaxation constraint $\det(\nabla\bar{\varphi}) = f(x)$ depends on the values of the function $f(x)$ over the entire image range Ω, so the transformation $\bar{\varphi}$ is non-local volume-preserving. Therefore, the choice of suitable ϕ is very important because it is a penalty measure to guarantee that $f(x)$ is positive, and it significantly affects the qualities of transformation grids as well as the image registration performance.
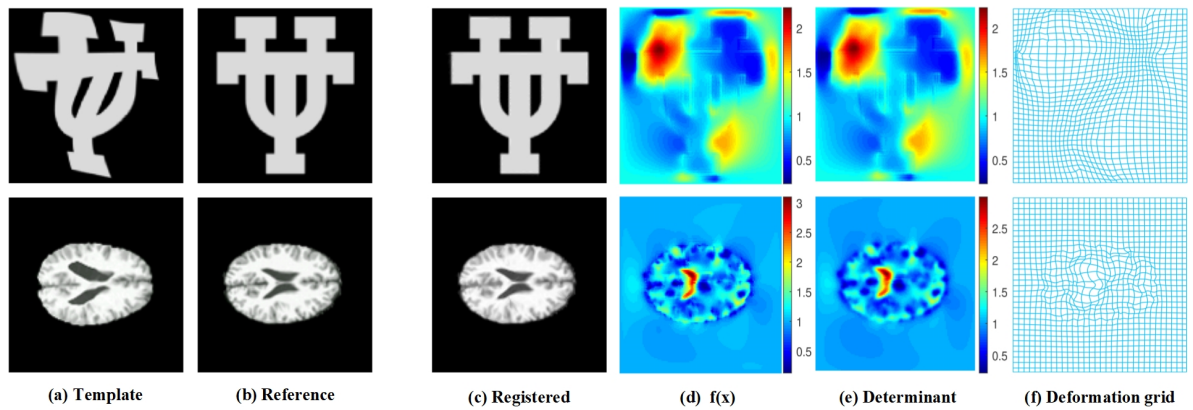
| (a) Template | (b) Reference | (c) Registered | (d) f(x) | (e) Determinant | (f) Deformation grid |

Figure 3: Registration of 2D images with penalty function ϕ_1: (a) template images; (b) reference images; (c) registered results; (d) the hotmap of $f(x)$; (e) the hotmap of the Jacobian determinant; (f) the deformation grids. Parameters of the two sets of images. UT(ϕ_1): $\tau_1 = 1.20$, $\tau_2 = 1e-03$, $\tau_3 = 5e-02$, $\lambda = 1.2$, $\rho = 1.2$, $\gamma = 120$; UT(ϕ_2): $\tau_1 = 1.40$, $\tau_2 = 1e-03$, $\tau_3 = 5e-02$, $\lambda = 1.2$, $\rho = 1.2$, $\gamma = 100$; Brain(ϕ_1): $\tau_1 = 0.32$, $\tau_2 = 1e-03$, $\tau_3 = 1e-02$, $\lambda = 0.6$, $\rho = 1.1$, $\gamma = 100$; Brain(ϕ_2): $\tau_1 = 0.32$, $\tau_2 = 1e-03$, $\tau_3 = 1e-02$, $\lambda = 0.6$, $\rho = 1.1$, $\gamma = 100$.

Table 1

Quantitative comparisons between registration results of both different penalty functions $\phi(\cdot)$. The best value is highlighted by the **bold**.

Examples	$\phi(\cdot)$	R_{min}	$\overline{\det}(J(\bar{\varphi}))$	$\det_{min}(J(\bar{\varphi}))$	$\det_{max}(J(\bar{\varphi}))$	*ssim*	Re_SSD	*psnr*
UT	ϕ_1	+	1.000	0.23	2.23	**0.9961**	**0.080%**	**35.49**
	ϕ_2	+	1.000	0.09	2.10	0.9953	0.083%	35.34
Brain	ϕ_1	+	1.000	0.22	3.00	**0.9868**	**2.67%**	**26.89**
	ϕ_2	+	1.000	0.30	2.78	0.9866	2.72%	26.81

Here, UT and Brain images with a resolution of 128×128 are used for this experiment. To make the comparison fairer, we set parameter configurations that make the registration results optimal for different penalty functions $\phi(\cdot)$. Table 1 presents the quantitative evaluations for the two penalty functions. Both schemes provide the corresponding diffeomorphic solutions with $R_{min} > 0$, and yield small ranges of volume changes. However, the differences between the models with different control functions are observable in several quantitative indicators. The penalty function ϕ_1 yields better Re_SSD, *ssim*, and *psnr* values. Therefore, we adopt the penalty function ϕ_1-based model as the default version throughout all following experiments.

Figure 3 evaluates the visualizations of the registered results obtained by the proposed model with penalty function ϕ_1, including the template and reference images, the transformed template images, the hotmaps of the relaxation function $f(x)$ and the Jacobian determinant $\det(\nabla \bar{\varphi})$, and the transformed grids. One can observe that the proposed scheme with ϕ_1 penalty term produces a transformed template that is visually identical to the reference, essentially the same hotmap distributions for the Jacobian determinant $\det(\nabla \bar{\varphi})$ and function $f(x)$,

A Bi-variant Variational Model for Diffeomorphic Image Registration with Relaxed Jacobian Determinant Constraints and smooth deformation grids. This also illustrates that the proposed method is robust to the heavy occlusion of illumination and large background clutters.

5.2. Sensitivity tests for the penalty parameter τ_2

The aim of using the penalty term $\int_\Omega \phi(f(\boldsymbol{x}))d\boldsymbol{x}$ of the relaxation function $f(\boldsymbol{x})$ is to prevent foldings and implausible volume change. In this part, we are interested in the contribution of the penalty term, we analyze it by setting the parameter τ_2 to zero or nonzero, while fixing all other optimal parameters. The effect of the term $\int_\Omega \phi(f(\boldsymbol{x}))d\boldsymbol{x}$ in modeling registration is assessed based on Circle-Square and Watermelon images with a resolution of 128×128 as well as BrainMR images with a resolution of 256×256.

Table 2

The relevant metrics are obtained from the three sets of experiments. "yes" and "no" represent the results of performing deformaton correction and not performing deformaton correction, respectively. The best value is highlighted by the **bold**.

Examples	τ_2	Correction	GFR	$\det_{\min}(J(\bar{\varphi}))$	$\det_{\max}(J(\bar{\varphi}))$	*ssim*	Re_SSD	*psnr*
	0	no	18.66%	-4.98	21.56	0.9981	0.052%	37.51
	0.01	no	3.17%	-1.00	14.09	0.9981	0.042%	38.40
Circle-Square	0	yes	0	0.03	5.21	0.9956	0.135%	33.33
	0.01	yes	0	0.75	1.95	**0.9984**	**0.036%**	**39.01**
	0	no	0.97%	-0.10	3.19	0.9530	0.892%	24.50
	0.001	no	0	0.34	2.17	**0.9620**	**0.695%**	**25.58**
Watermelon	0	yes	0	0.08	3.88	0.9571	0.780%	25.07
	0.001	yes	0	0.34	2.17	**0.9620**	**0.695%**	**25.58**
	0	no	2.44%	-11.30	21.64	0.9550	7.904%	16.99
	0.001	no	0	0.07	8.67	**0.9651**	**3.699%**	**20.25**
BrainMR	0	yes	0	0.02	15.96	0.9601	3.998%	19.90
	0.001	yes	0	0.30	8.12	0.9648	3.785%	20.16

To discuss the influence of the penalty term, we first perform numerical experiments using $\tau_2 = 0$ and $\tau_2 \neq 0$ without imposing deformation correction, and then conduct the same experiments with deformation correction. In particular, we compare the indicator of grid folding ratio in the experiments. Table 2 presents how the registration results are affected with and without using the penalty term $\int_\Omega \phi(f(\boldsymbol{x}))d\boldsymbol{x}$. It can be seen from Table 2 that the local grid folding cases ($\det_{\min}(J(\bar{\varphi})) < 0$ or GPR > 0) are presented in all three examples without imposing the deformation correction when the hyper-parameter $\tau_2 = 0$ of the function $\phi(\cdot)$ is already fixed. Compared with it, the grid folding ratio can be reduced or eliminated when $\tau_2 \neq 0$, and the registration accuracy can be improved. However, the grid folding still occurs when using the penalty term in the Circle-Square example. As has been pointed out in Remark 1, the unsuitable choices of hyper-parameters and the unsatisfactory numerical solution
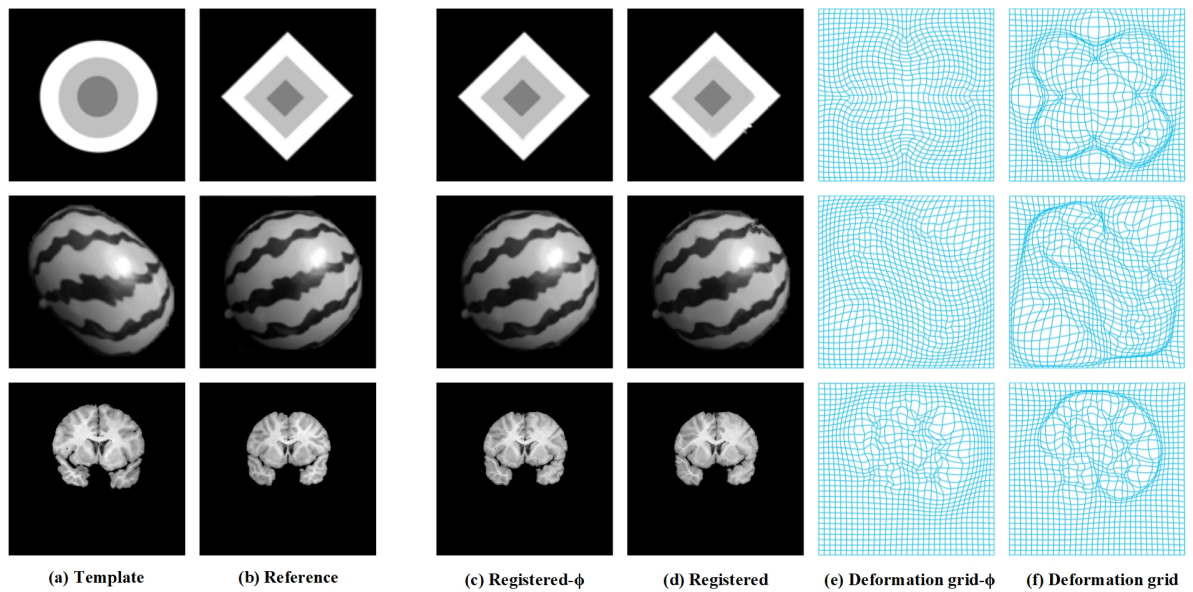
(a) Template (b) Reference (c) Registered-ϕ (d) Registered (e) Deformation grid-ϕ (f) Deformation grid

Figure 4: Registration results with and without control function using the deformaton correction: (a) template images; (b) reference images; (c) registered images with control function; (d) registered images without control function; (e)-(f) a visualization of the deformed grids with and without control function. Parameters of the three sets of images. Circle-Square: $\tau_1 = 0.3$, $\tau_2 = 1e-02$, $\tau_3 = 1e-03$, $\lambda = 0.8$, $\rho = 1.08$, $\gamma = 18$; Watermelon: $\tau_1 = 0.2$, $\tau_2 = 1e-03$, $\tau_3 = 1e-03$, $\lambda = 1.06$, $\rho = 1.06$, $\gamma = 16$; BrainMR: $\tau_1 = 0.4$, $\tau_2 = 5e-03$, $\tau_3 = 1e-03$, $\lambda = 0.4$, $\rho = 1.16$, $\gamma = 20$.

technique of nonlinear equation in practice may result in $f(\boldsymbol{x}) < 0$, which leads to grid folding. Moreover, the grid correction in Algorithm 1 can be employed to generate a desirable diffeomorphic deformation.

Next, we illustrate the registration results for three examples with or without the penalty term $\int_{\Omega} \phi(f(\boldsymbol{x})) d\boldsymbol{x}$ where the deformation correction is adopted. As illustrated in Figure 4, the proposed model with the penalty term not only generates better registered images but also produces smoother and more realistic transformations. The reasons are two-fold. Firstly, the penalty term limits the range of $f(\boldsymbol{x})$ to be near 1 as far as possible, and indirectly determines the range of $\det\left(\nabla\bar{\boldsymbol{\varphi}}(\boldsymbol{x})\right)$. Secondly, the more smoother nature of the image deformation is strongly required in practice, the regulariztion term $\int_{\Omega} |\nabla f(\boldsymbol{x})|^2 d\boldsymbol{x}$ in this work ensures the smoothness of $f(\boldsymbol{x})$, which also relate to smoothness of the transformation $\bar{\boldsymbol{\varphi}}(\boldsymbol{x})$. These confirm that the penalty term with the relaxation function $f(\boldsymbol{x})$ is important for the proposed model, which makes the deformation smoother and tends to volume-preserving.

5.3. Comparisons for algorithm convergence

We further compare the proposed algorithm with the diffusion- and curvature-based registration algorithms to demonstrate the convergence and volume-preserving using the IC example. For fair, all three methods are iterated 100 steps at each level. In Figure 5, we plot the change curves of the similarity measure $D(\boldsymbol{u})$, relative objective function $\hat{\mathcal{L}}^{\ell,k} := \frac{\mathcal{L}^{\ell,k}}{\mathcal{L}^{L,1}}$ ($\mathcal{L}^{\ell,k}$ represents the objective function value of the k-th iteration at the ℓ-th level and $\mathcal{L}^{L,1}$ represents the initial objective function value of the coarsest L-th level), and average Jacobian determinant
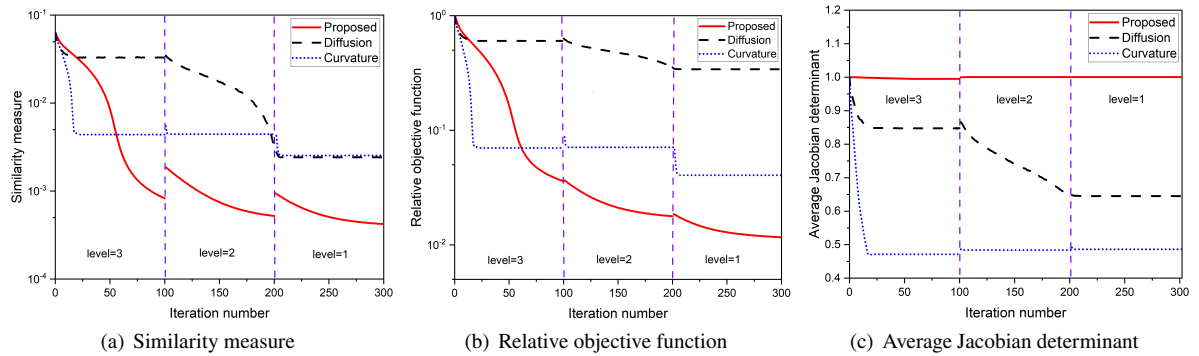
Figure 5: Convergence and volume-preserving comparisons of the proposed, diffusion, and curvature models for the IC example. (a) similarity measure $\mathcal{D}(\boldsymbol{u})$ (the y-coordinate is logarithmic); (b) relative objective function $\hat{\mathcal{L}}^{\ell,k}$ (the y-coordinate is logarithmic); (c) average Jacobian determinant $\overline{\det}(J(\bar{\boldsymbol{\varphi}}))$. The red solid, black dash, and blue dot lines indicate the results of the proposed, diffusion, and curvature models, respectively.

$\overline{\det}(J(\bar{\boldsymbol{\varphi}}))$ of three methods with respective to the number of iterations. From Figure 5(a)-(b), we observe that the similarity measure and relative objective function value of the proposed algorithm decreased monotonically at each level and gradually stabilized. This indicates that the proposed algorithm is converged. Although the diffusion and curvature methods converge faster than that of the proposed method, their similarity measures and relative objective function values are worse than ours. This means that our method is more satisfactory. Moreover, it can be seen from Figure 5(c) that the proposed algorithm can guarantee $\overline{\det}(J(\bar{\boldsymbol{\varphi}})) \approx 1$, which is consistent with the conclusion of volume-preserving in the average sense.

5.4. Comparisons to diffusion- and curvature-based methods

In this part, we validate the proposed diffeomorphic registration method using IC image of size 200×200, Lena and Hand images of size 128×128 as three sets of examples. Our results are compared quantitatively and qualitative with the diffusion and curvature registration methods described in [42]. Here, we use a multilevel strategy ($L = 3$) and set MaxIter $= 200$ for all models.

In Figure 6 and Figure 7, we compare the visualizations of the registered results obtained by the proposed model with the diffusion and curvature registrations, including the template and reference images with zoom-in regions, the transformed template images, the registration errors of $T(\bar{\boldsymbol{\varphi}}) - R(\boldsymbol{x})$, the hotmaps of the Jacobian determinant $\det(\nabla\bar{\boldsymbol{\varphi}})$, and transformations $\bar{\boldsymbol{\varphi}}$. In our model, all three examples produce desirable registration results where the diffeomorphism of the transformations is kept. However, one can observe that the diffusion and curvature models failed to obtain a good registration for the IC and Lena examples (*see* the zoom-in regions in Figure 6(b)). In particular, the transformation grids of the two models are seriously folding for the IC example. Moreover, it can be found by observing the deformation of Lena and Hands examples that the deformation generated by the curvature model is smoother than ours. The main reason is that the curvature model applied
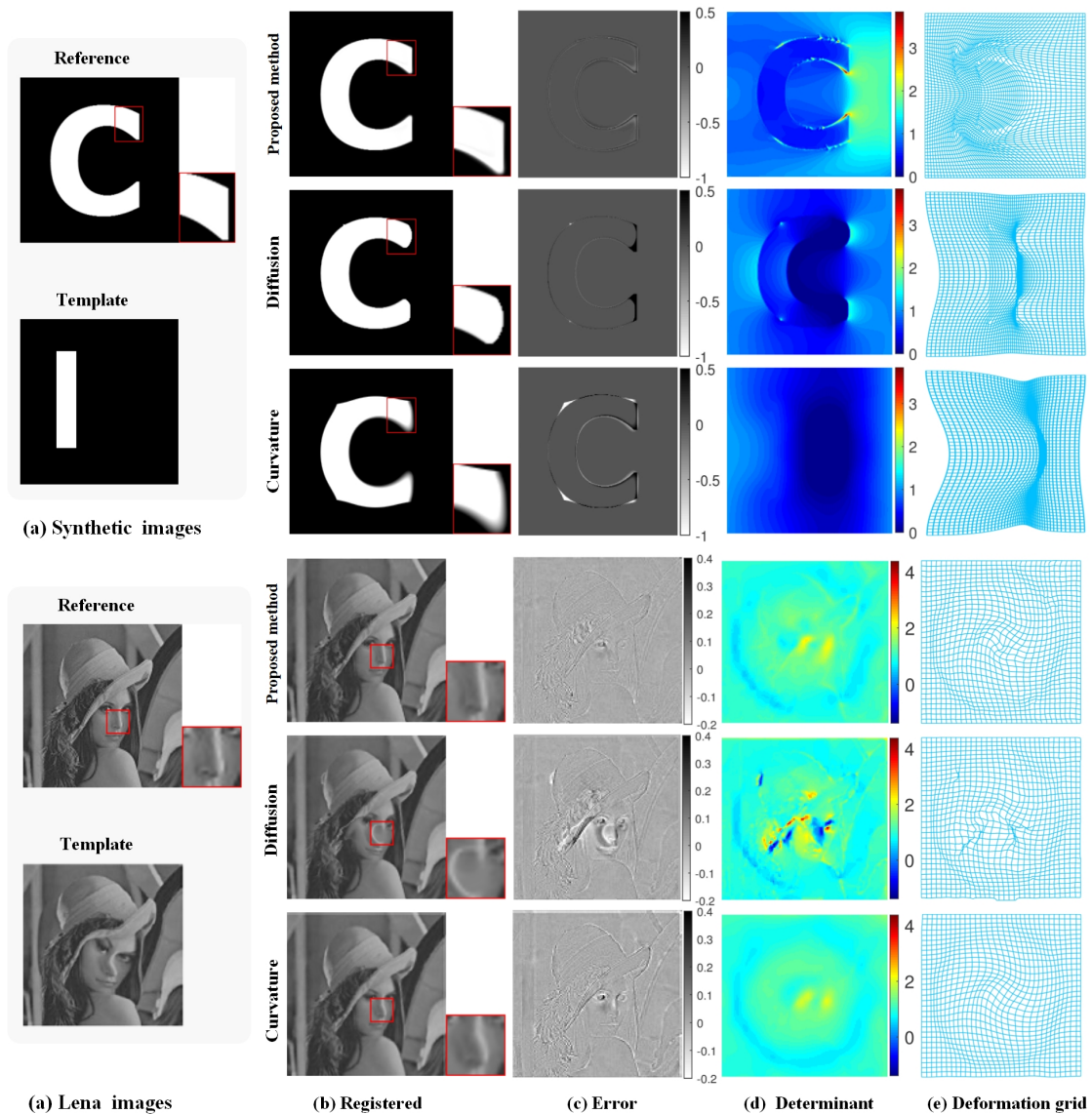
Figure 6: Comparisons of the proposed, diffusion, and curvature models. (a) the reference and template images (Synthetic and Lena); (b) the deformed template images of the three classical models with the optimal parameters (Synthetic: $\tau_1 = 3$, $\tau_2 = 1e-2$, $\tau_3 = 1e-3$, $\lambda = 1$, $\gamma = 100$, $\rho = 1.06$ for the proposed model; $\alpha = 8800$ for diffusion model; $\alpha = 200$ for curvature model. Lena: $\tau_1 = 0.6$, $\tau_2 = 1e-2$, $\tau_3 = 1e-3$, $\lambda = 0.2$, $\gamma = 200$, $\rho = 1.02$ for the proposed model; $\alpha = 400$ for the diffusion model; $\alpha = 1$ for curvature model); (c) the registration errors of $T(\bar{\varphi}) - R(\boldsymbol{x})$; (d) the Jacobian determinant hotmaps of the deformation fields; (e) the deformation grids.

the second-order derivatives to the regulariztion of the displacement field, while our regularizer considers the first-order derivatives.
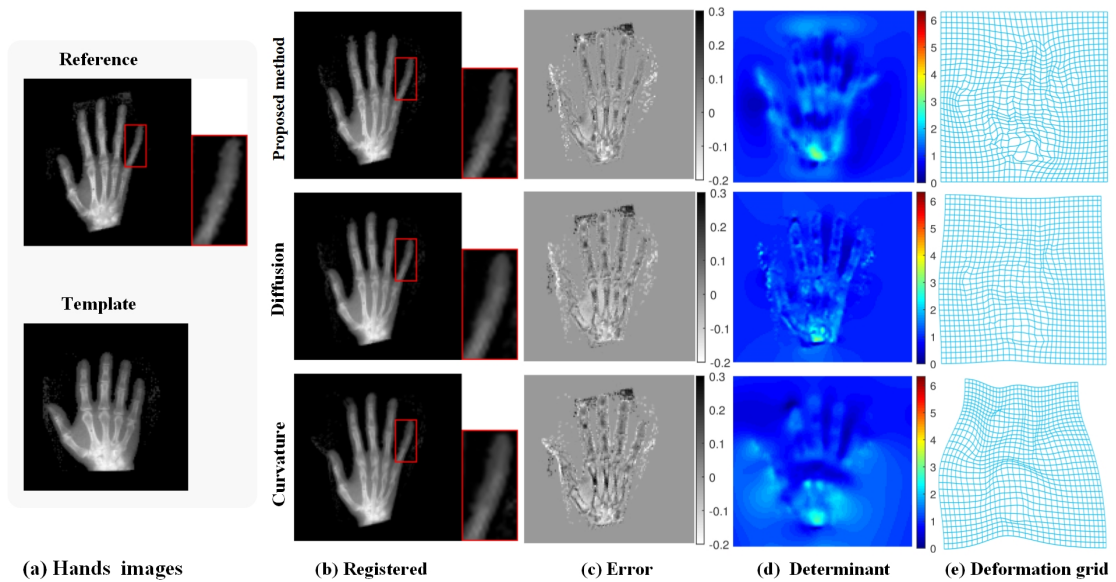
Figure 7: Comparisons of the proposed, diffusion, and curvature models. (a) the reference and template images; (b) the registered results of the three classical models with the optimal parameters (Hands: $\tau_1 = 0.4$, $\tau_2 = 1e-2$, $\tau_3 = 1e-3$, $\lambda = 0.2$, $\gamma = 400$, $\rho = 1.02$ for the proposed model; $\alpha = 500$ for diffusion model; $\alpha = 0.2$ for the curvature model); (c) the registration errors of $T(\bar{\varphi}) - R(x)$; (d) the Jacobian determinant hotmaps of the deformation fields; (e) the deformation grids.

Table 3

The quantitative evaluation comparisons of the proposed, diffusion, and curvature models. The negative Jacobian and best metrics values are highlighted by the <u>underline</u> and **bold**.

Examples	Methods	$\overline{\det}(J(\bar{\varphi}))$	R_{min}	$\det_{min}(J(\bar{\varphi}))$	$\det_{max}(J(\bar{\varphi}))$	*ssim*	Re_SSD	*psnr*
IC	Proposed	0.999	+	0.29	3.84	**0.9828**	**0.23%**	**27.85**
	Diffusion	0.677	−	<u>-0.30</u>	1.70	0.9775	3.51%	15.80
	Curvature	0.504	−	<u>-0.14</u>	1.07	0.9553	3.67%	15.73
Lena	Proposed	0.999	+	0.46	3.09	**0.9193**	**3.31%**	**25.09**
	Diffusion	1.013	−	<u>-1.39</u>	4.38	0.8614	8.05%	21.23
	Curvature	1.012	+	0.56	2.02	0.8520	7.86%	21.35
Hands	Proposed	1.000	+	0.32	6.33	**0.8943**	**3.04%**	**18.46**
	Diffusion	1.008	−	<u>-0.09</u>	3.34	0.8845	4.20%	17.14
	Curvature	1.011	−	<u>-0.05</u>	2.81	0.8829	5.00%	16.24

In Table 3, we can see that there are significant portions of transformations where the global volume-preserving assumption (i.e., $\overline{\det}(J(\bar{\varphi})) = 1$) is reasonable, and even object in template that is smaller than one in reference, such as IC example, has been successfully registered as such for the purpose of analysis and inference. We can also observe that the diffeomorphism principle $\det(\nabla\bar{\varphi}) > 0$ is clearly violated when the diffusion-based and curvature-based methods are applied in many manual and natural images. By using the diffusion-based model, Table 3
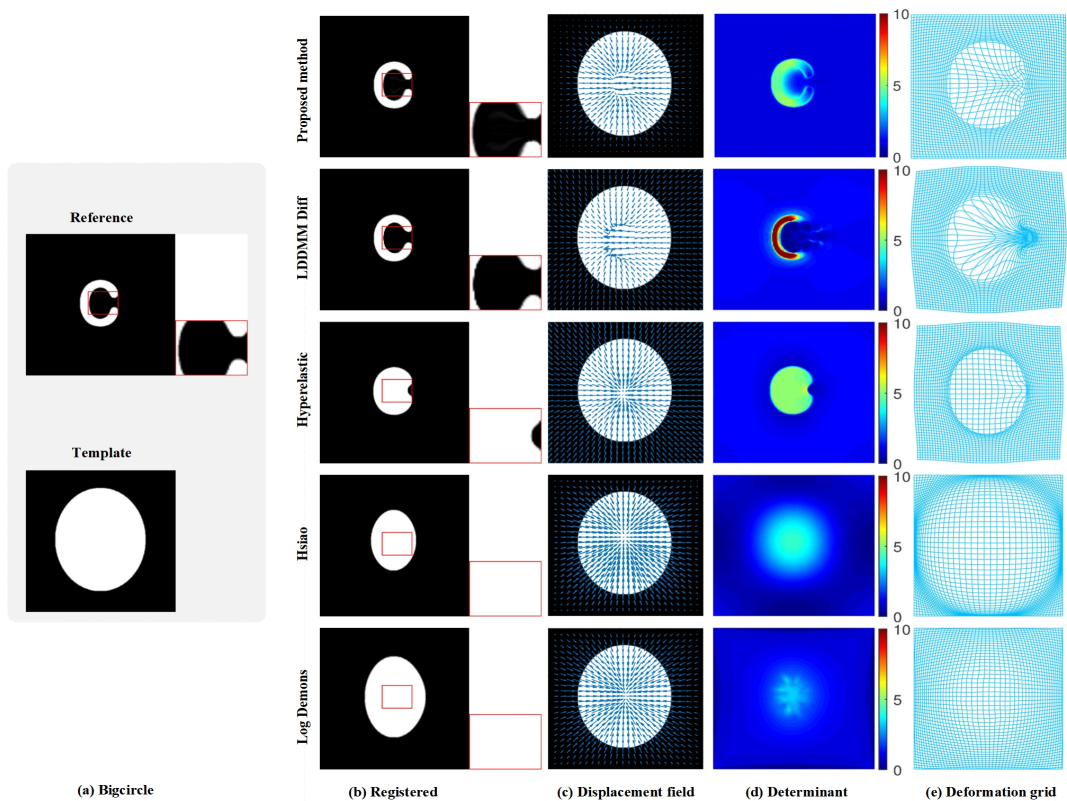
Figure 8: Comparisons of diffeomorphic models for the Bigcircle example. (a) the reference and template images (Bigcircle example); (b) the registered results of these models with the optimal parameters (Bigcircle: $\tau_1 = 2.2$, $\tau_2 = 2e-2$, $\tau_3 = 1e-3$, $\lambda = 1$, $\gamma = 160$, $\rho = 1.02$ for the proposed model, $\alpha = 650$ for the LDDMM model, $\alpha_1 = 18$, $\alpha_2 = 90$, $\alpha_3 = 0$, $\alpha_4 = 6$ for the Hyper-elastic model, $\sigma_{fluid} = 2.6$, $\sigma_{diffusion} = 1.3$, $\sigma_i = 1$, $\sigma_x = 2$ for the Log Demons model); (c) the displacement fields; (d) the Jacobian determinant hotmaps; (e) the deformation grids.

numerically shows $\det(\nabla\bar{\varphi}) \in [-0.3, 1.7]$ in the IC example, $\det(\nabla\bar{\varphi}) \in [-1.39, 4.38]$ in the Lena example, and $\det(\nabla\bar{\varphi}) \in [-0.09, 3.34]$ in the Hands example, which illustrates that $\bar{\varphi}$ is not diffeomorphic. The curvature registration also generates nondiffeomorphic mapping $\bar{\varphi}$ for the IC and Hands examples. But the proposed model not only yields the diffeomorphic transformations with $\det(\nabla\bar{\varphi}) \in [0.29, 3.84]$, $\det(\nabla\bar{\varphi}) \in [0.46, 3.09]$, and $\det(\nabla\bar{\varphi}) \in [0.32, 6.33]$ for the three examples, but also achieves best Re_SSD, *ssim*, and *psnr* scores. The results demonstrate that the proposed method can prevent the grid folding and achieve very good registration performance.

5.5. Comparisons with other diffeomorphic models

In this part, we also conducted the registration experiments of the popular diffeomorphic models on Bigcircle, Pineapple, and Abdomen images (the resolution of the Bigcircle example is 200×200 and the other two examples are 128×128). We compare our approach with the state-of-the-art diffeomorphic models including Hyper-elastic [6], LDDMM [41], Log Demons [40], and Hsiao model [33]. For all registration models, we use a L-level multilevel strategy ($L = 5$) and set MaxIter $= 100$.

Table 4

The quantitative evaluation comparisons of the proposed and diffeomorphic models. The best metrics values are highlighted by the **bold**.

Examples	Methods	$\overline{\det}(J(\bar{\varphi}))$	R_{min}	$\det_{min}(J(\bar{\varphi}))$	$\det_{max}(J(\bar{\varphi}))$	ssim	Re_SSD	psnr	Time(s)
	Proposed	1.004	+	0.70	5.56	0.9652	**0.08**%	**21.93**	10.77
	LDDMM	2.665	+	0.05	*39.88*	**0.9905**	0.33%	15.88	27.33
Bigcircle	Hyperelastic	1.935	+	0.14	6.02	0.9436	9.48%	3.86	34.96
	Log Demons	1.293	+	0.003	3.25	0.7908	48.68%	1.14	11.53
	Hsiao	2.011	+	0.001	4.22	0.8819	19.42%	2.32	52.43
	Proposed	1.001	+	0.24	3.65	**0.9770**	**0.26**%	**31.16**	4.71
	LDDMM	1.072	+	0.11	3.73	0.9538	1.06 %	25.03	4.20
Pineapple	Hyperelastic	1.040	+	0.06	2.53	0.9244	1.75%	22.84	22.66
	Log Demons	1.112	+	0.002	3.40	0.8955	1.52 %	19.49	6.02
	Hsiao	1.077	+	0.38	2.11	0.8178	9.06%	15.66	17.47
	Proposed	1.000	+	0.51	2.32	**0.9516**	**3.53**%	**17.91**	5.40
	LDDMM	0.958	+	0.12	6.27	0.9227	7.62%	14.44	5.79
Abdomen	Hyperelastic	0.944	+	0.20	2.63	0.9146	8.49%	13.95	24.01
	Log Demons	1.023	+	0.58	1.86	0.8997	7.86%	12.37	7.21
	Hsiao	1.027	+	0.65	1.50	0.8763	13.43%	11.97	17.03

The registered results in Figure 8-Figure 10 clearly show the effectiveness of the proposed method over the other four methods. As can be apparently seen from the Figure 8, Hyper-elastic, Log Demons, and Hsiao models fail to register the alphabet C. Although LDDMM presents an acceptable result, it produces a drastic volume change. However, the proposed method perfectly registers the sharp edges of the large deformation image and produces a smooth deformation, which can be observed from the visualization of deformation grid in Figure 8(e). Besides, Figure 9(b)-Figure 10(b) illustrate that the proposed method is better at "low-contrast" regions registration. The zoom-in regions show that inner structure of the registered images obtained by our method are almost the ground truth reference images. While the other four methods have not given satisfactory registration results.

To further validate the effectiveness of our approach, we evaluate the average value of the Jacobian determinant $\overline{\det}(J(\bar{\varphi}))$, the range of the Jacobian determinant, and registration accuracy. In Table 4, all the methods yield diffeomorphic transformations. It is worth noting that the average Jacobian determinant obtained by our approach is closest to 1. Also, compared with LDDMM and Hyper-elastic methods, our approach almost has a smaller range for the Jacobian determinant, such as $\det(\nabla\bar{\varphi}) \in [0.05, 39.88]$ of LDDMM, $\det(\nabla\bar{\varphi}) \in [0.14, 6.02]$ of Hyper-elastic, and $\det(\nabla\bar{\varphi}) \in [0.70, 5.56]$ of the proposed model for the Bigcircle example. This is because
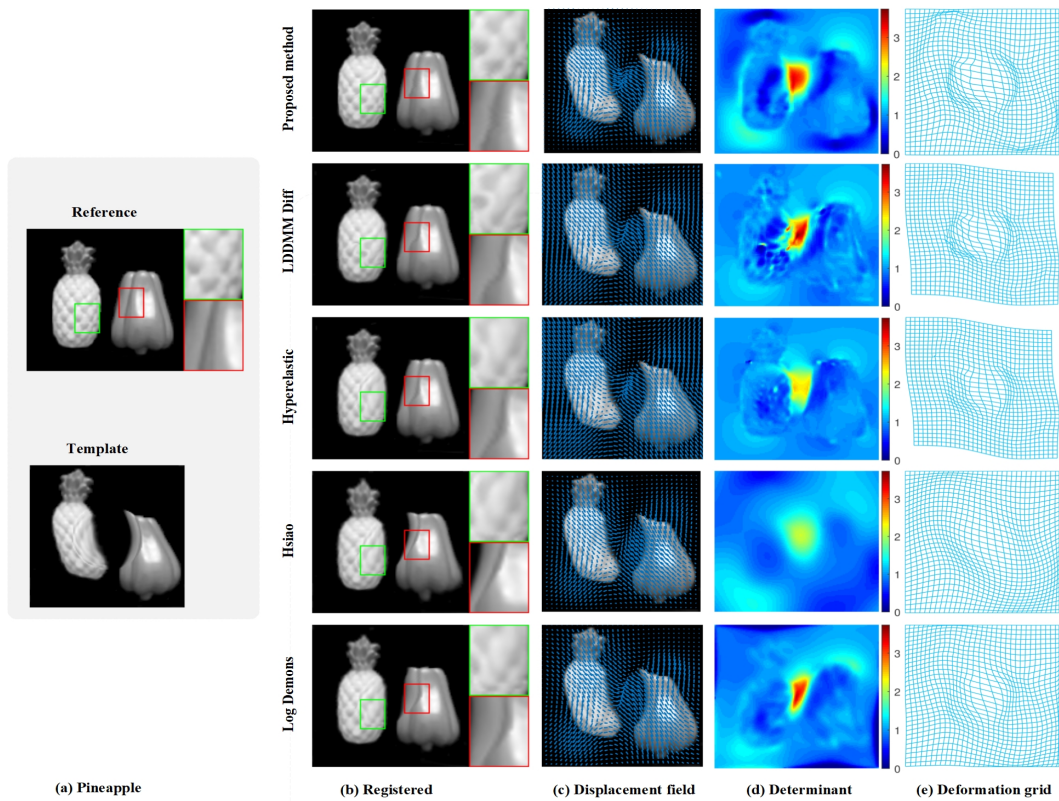
Figure 9: Comparisons of diffeomorphic models for the Pinealpple example. (a) the reference and template images; (b) the registered results of these models with the optimal parameters (Pinealpple: $\tau_1 = 0.2$, $\tau_2 = 1e-3$, $\tau_3 = 1e-4$, $\lambda = 0.08$, $\gamma = 130$, $\rho = 1.01$ for the proposed model, $\alpha = 100$ for the LDDMM model, $\alpha_1 = 28$, $\alpha_2 = 22$, $\alpha_3 = 0$, $\alpha_4 = 1$ for the Hyper-elastic model, $\sigma_{fluid} = 2.2$, $\sigma_{diffusion} = 1.2$, $\sigma_i = 1$, $\sigma_x = 2$ for the Log Demons model); (c) the displacement fields; (d) the Jacobian determinant hotmaps; (e) the deformation grids.

the proposed model explicitly controls and penalizes volume change so that deformation tends to be volume-preserving and is smoother. Furthermore, the proposed method obtains significantly state-of-the-art results by comparing to Re_SSD, *ssim*, and *psnr* scores. In particular, our approach obtains the best Re_SSD of 0.08% and psnr of 21.93 for the Bigcircle example. On the other hand, the proposed method has competitive advantages in terms of registration time; especially the proposed and LDDMM methods have less time overheads for the Pineapple and Abdomen examples. In conclusion, many such comparisons confirm the superiority of our approach over these state-of-the-art diffeomorphic registration models in terms of the capability of accurately handling large deformations and the volume-preserving in the average sense.
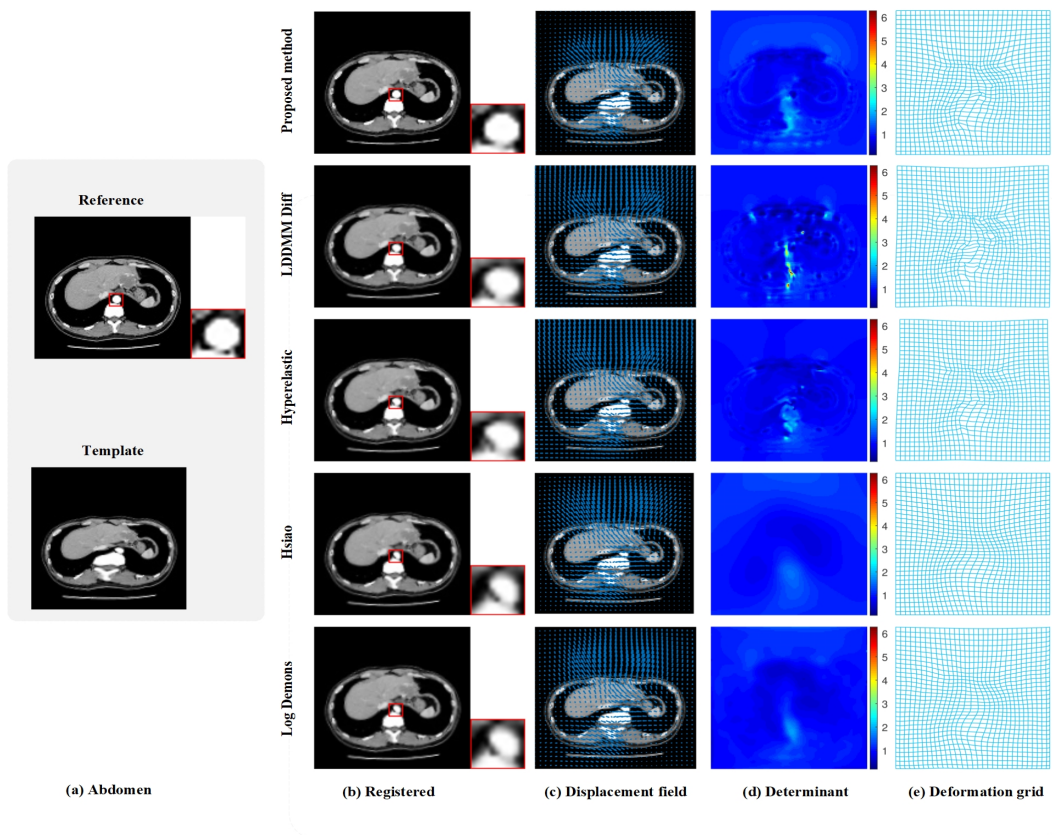
Figure 10: Comparisons of diffeomorphic models for the Abdomen example. (a) the reference and template images; (b) the registered results of these models with the optimal parameters (Abdomen: $\tau_1 = 1.4$, $\tau_2 = 1e-2$, $\tau_3 = 1e-2$, $\lambda = 2$, $\gamma = 220$, $\rho = 1.02$ for the proposed model, $\alpha = 30$ for the LDDMM model, $\alpha_1 = 16$, $\alpha_2 = 20$, $\alpha_3 = 0$, $\alpha_4 = 1$ for the Hyper-elastic model, $\sigma_{fluid} = 2.6$, $\sigma_{diffusion} = 0.6$, $\sigma_i = 1$, $\sigma_x = 2$ for the Log Demons model); (c) the displacement fields; (d) the Jacobian determinant hotmaps; (e) the deformation grids.

Table 5

The quantitative evaluation comparisons of the proposed and diffeomorphic models for 3D experiment. The best metrics values are highlighted by the bold.

Example	Methods	$\overline{\det(J(\bar{\varphi}))}$	R_{min}	$\det_{\min}(J(\bar{\varphi}))$	$\det_{\max}(J(\bar{\varphi}))$	*ssim*	Re_SSD	*psnr*	Time(s)
	Proposed	1.000	+	0.2201	2.26	**0.9865**	**2.25%**	**24.64**	1091.96
	LDDMM	0.959	+	0.0008	3.14	0.9822	3.19%	22.99	1961.95
Brain	Log Demons	1.001	+	0.0315	2.80	0.8368	22.13%	14.90	398.43
	Hsiao	1.001	+	0.6881	2.08	0.8560	25.46%	14.18	4698.91

5.6. 3D registration experiment

In Figure 11 and Table 5, we compare our approach with state-of the-art diffeomorphic methods including LDDMM, Log Demons, and Hsiao models when tested on Brain images of $128 \times 128 \times 128$. In this experiment, we use a multilevel strategy ($L = 5$) and set MaxIter $= 200$ for all models.

(a) 3D Brain images

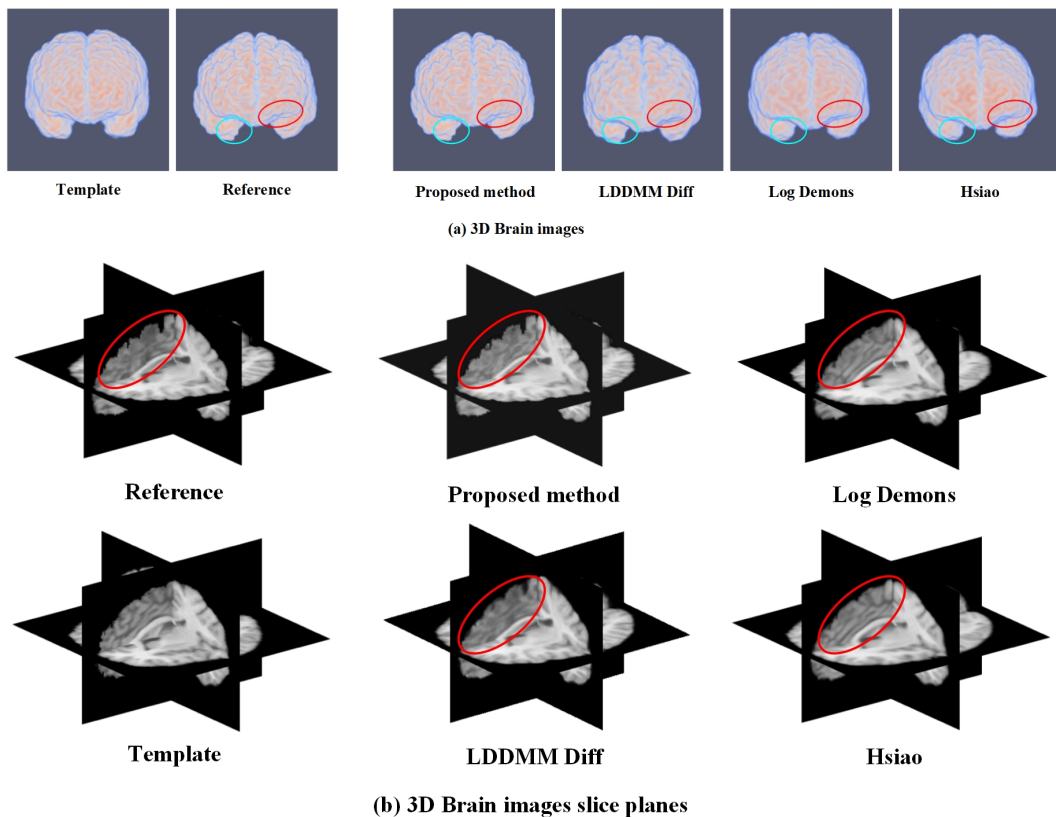
(b) 3D Brain images slice planes

Figure 11: 3D visualization of the registration problem for the brain images. (a) shows the reference image, template image and deformed template images generated by these four models. (b) visualize the registered images from slice planes.

By observing the texture and sharp edges of the brain surface in Figure 11 (*see* marked elliptical region), we can see that the registration results of our scheme are closer to the reference image than those of other methods. This demonstrates that our method has more advantages in dealing with complicated details. The results in Table 5 show that all methods produce diffeomorphic transformations while our approach has a relatively small Jacobian determinant varying range ($\det(\nabla\bar{\varphi}) \in [0.22, 2.26]$). As illustrated in Table 5, the proposed model can consistently achieve the best values for the Re_SSD, *ssim*, and *psnr* scores. In addition, the Log Demons method has the lowest time cost because it does not need to solve the system of linear equations, which is usually the computational bottleneck of large-scale 3D registration problems. Among the remaining methods, the proposed method has a lower time cost, taking only 1091.96 seconds. Hence, this example demonstrates that our approach can be applied to 3D image registration problems, and produce the top-ranked results with diffeomorphic transformations and small volume change.

6. Conclusions

In this paper, we propose a novel registration model with the relaxation constraint of Jacobian equation $\det(\nabla\boldsymbol{\varphi}(\boldsymbol{x})) = f(\boldsymbol{x}) > 0$ to obtain smooth and diffeomorphic mapping for the large transformation image registration problems. We note that the relaxation function $f(\boldsymbol{x})$ can limit the range of the Jacobian determinant $\det(\nabla\boldsymbol{\varphi}(\boldsymbol{x}))$. Thus, instead of controlling the Jacobian determinant of the transformation directly, controlling $f(\boldsymbol{x})$ is also a good alternative providing the same but indirect control. To obtain diffeomorphic and volume-preserving deformation, we propose a novel penalty term $\int_\Omega \phi(f(\boldsymbol{x}))d\boldsymbol{x}$ to control the relaxation function automatically so that $f(\boldsymbol{x})$ is positive and as close to one as possible. Also, we present a regularization term $\int_\Omega |\nabla f(\boldsymbol{x})|^2 d\boldsymbol{x}$ to improve the smoothness of $f(\boldsymbol{x})$, thereby indirectly enhancing the smoothness of deformation. Furthermore, we analyze the existence of the optimal solution for the proposed variational model and provide a numerical algorithm for the model which combines penalty splitting and multilevel schemes. This algorithm can also detect grid foldings and automatically correct them. Finally, numerical experiments show that the proposed model with the penalty term can generates volume-preserving on average and smoother transformation, and the convergence comparisons of our algorithm with other algorithms are illustrated. Compared with the classical registration models, the proposed model produces diffeomorphic transformations and obtains better performance for the large deformation 2D and 3D images. In future work, we will extend our scheme to multimodal registration model.

Acknowledgments

CRediT authorship contribution statement

Yanyan Li: Conceptualization, Software, Validation, Writing-Original Draft, Writing-Review and Editing. **Ke Chen:** Conceptualization, Validation, Methodology, Writing-Review and Editing. **Chong Chen:** Conceptualization, Validation, Methodology, Writing-Review and Editing. **Jianping Zhang:** Conceptualization, Supervision, Methodology, Writing-Review and Editing, Funding acquisition.

References

[1] Arsigny, V., Commowick, O., Pennec, X., Ayache, N., 2006. A log-Euclidean framework for statistics on diffeomorphisms, in: Med. Image Comput. Comput. Assist. Interv., pp. 924–931. doi:https://doi.org/10.1007/11866565_113.

[2] Ashburner, J., Friston, K.J., 2011. Diffeomorphic registration using geodesic shooting and Gauss-Newton optimisation. NeuroImage 55, 954–967. doi:https://doi.org/10.1016/j.neuroimage.2010.12.049.

[3] Aubert, G., Kornprobst, P., 2006. Mathematical Problems in Image Processing: Partial Differential Equations and the Calculus of Variations. 2nd ed., Springer Publishing Company, Incorporated.

[4] Bauer, M., Joshi, S., Modin, K., 2015. Diffeomorphic density matching by optimal information transport. SIAM J. Imaging Sci. 8, 1718–1751. doi:https://doi.org/10.1137/151006238.

[5] Beg, M.F., Miller, M.I., Trouvé, A., Younes, L., 2005. Computing large deformation metric mappings via geodesic flows of diffeomorphisms. Int. J. Comput. Vis. 61, 139–157. doi:https://doi.org/10.1023/B:VISI.0000043755.93987.aa.

[6] Burger, M., Modersitzki, J., Ruthotto, L., 2013. A hyperelastic regularization energy for image registration. SIAM J. Sci. Comput. 35, B132–B148. doi:https://doi.org/10.1137/110835955.

[7] Charon, N., Trouvé, A., 2013. The varifold representation of nonoriented shapes for diffeomorphic registration. SIAM J. Imaging Sci. 6, 2547–2580. doi:https://doi.org/10.1137/130918885.

[8] Chen, C., 2021. Spatiotemporal imaging with diffeomorphic optimal transportation. Inverse Probl. 37, 115004. doi:https://doi.org/10.1088/1361-6420/ac2a91.

[9] Chen, C., Gris, B., Öktem, O., 2019. A new variational model for joint image reconstruction and motion estimation in spatiotemporal imaging. SIAM J. Imaging Sci. 12, 1686–1719. doi:https://doi.org/10.1137/18M1234047.

[10] Chen, C., Öktem, O., 2018. Indirect image registration with large diffeomorphic deformations. SIAM J. Imaging Sci. 11, 575–617. doi:https://doi.org/10.1137/17M1134627.

[11] Christensen, G., Rabbitt, R., Miller, M., 1996. Deformable templates using large deformation kinematics. IEEE Trans. Image Process. 5, 1435–1447. doi:https://doi.org/10.1109/83.536892.

[12] Chumchob, N., 2010. A variational approach for discontinuity-preserving image registration. East-West J. Math.. 2010, 266–282.

[13] Chumchob, N., Chen, K., Brito-Loeza, C., 2011. A fourth-order variational image registration model and its fast multigrid algorithm. Multiscale Model. Simul. 9, 89–128. doi:https://doi.org/10.1137/100788239.

[14] Collignon, A., Maes, F., Delaere, D., Vandermeulen, D., Suetens, P., Marchal, G., 1995. Automated multi-modality image registration based on information theory, in: Inf. Process. Med. Imaging, pp. 263–274.

[15] D'Agostino, E., Maes, F., Vandermeulen, D., Suetens, P., 2003. A viscous fluid model for multimodal non-rigid image registration using mutual information. Med. Image. Anal. 7, 565–575. doi:https://doi.org/10.1016/S1361-8415(03)00039-2.

[16] Dalca, A.V., Balakrishnan, G., Guttag, J., Sabuncu, M.R., 2018. Unsupervised learning for fast probabilistic diffeomorphic registration, in: Med. Image Comput. Comput. Assist. Interv., pp. 729–738. doi:https://doi.org/10.1007/978-3-030-00928-1_82.

[17] Dupuis, P., Grenander, U., Miller, M.I., 1998. Variational problems on flows of diffeomorphisms for image matching. Q. Appl. Math. 56, 587–600.

[18] Feydy, J., Charlier, B., Vialard, F.X., Peyré, G., 2017. Optimal transport for diffeomorphic registration, in: Med. Image Comput. Comput. Assist. Interv., pp. 291–299. doi:https://doi.org/10.1007/978-3-319-66182-7_34.

[19] Fischer, B., Modersitzki, J., 2002. Fast diffusion registration. Contemp. Math. 313, 117–127. doi:https://doi.org/10.1090/conm/313/05372.

[20] Fischer, B., Modersitzki, J., 2003. Curvature based image registration. J. Math. Imaging Vis. 18, 81–85. doi:https://doi.org/10.1023/A:1021897212261.

[21] Fischer, B., Modersitzki, J., 2004. A unified approach to fast image registration and a new curvature based registration technique. Linear Algebra Appl. 380, 107–124. doi:https://doi.org/10.1016/j.laa.2003.10.021.

[22] Fischler, M., Elschlager, R., 1973. The representation and matching of pictorial structures. IEEE Trans. Comput. C-22, 67–92. doi:https://doi.org/10.1109/T-C.1973.223602.

[23] Frohn-Schauf, C., Henn, S., Witsch, K., 2007. Multigrid based total variation image registration. Comput. Vis. Sci. 11, 101–113. doi:https://doi.org/10.1007/s00791-007-0060-2.

[24] Guo, Y., Chen, Q., Choi, G.P., Lui, L.M., 2023. Automatic landmark detection and registration of brain cortical surfaces via quasi-conformal geometry and convolutional neural networks. Comput. Biol. Med. 163, 107185. doi:https://doi.org/10.1016/j.compbiomed.2023.107185.

[25] Haber, E., Modersitzki, J., 2004. Numerical methods for volume preserving image registration. Inverse Probl. 20, 1621–1638. doi:https://doi.org/10.1088/0266-5611/20/5/018.

[26] Haber, E., Modersitzki, J., 2006. Image registration with guaranteed displacement regularity. Int. J. Comput. Vis. 71, 361–372. doi:https://doi.org/10.1007/s11263-006-8984-4.

[27] Han, H., Wang, Z., 2020. A diffeomorphic image registration model with fractional-order regularization and Cauchy–Riemann constraint. SIAM J. Imaging Sci. 13, 1240–1271. doi:https://doi.org/10.1137/19M1260621.

[28] Han, H., Wang, Z., Zhang, Y., 2021. Multiscale approach for two-dimensional diffeomorphic image registration. Multiscale Model. Simul. 19, 1538–1572. doi:https://doi.org/10.1137/20M1383987.

[29] Henn, S., 2006. A full curvature based algorithm for image registration. J. Math. Imaging Vis. 24, 195–208. doi:https://doi.org/10.1007/s10851-005-3621-3.

[30] Hering, A., Häger, S., Moltz, J., Lessmann, N., Heldmann, S., van Ginneken, B., 2021. CNN-based lung CT registration with multiple anatomical constraints. Med. Image. Anal. 72, 102139. doi:https://doi.org/10.1016/j.media.2021.102139.

[31] Hermosillo, G., Chefd'Hotel, C., Faugeras, O., 2002. Variational methods for multimodal image matching. Int. J. Comput. Vis. 50, 329–343. doi:https://doi.org/10.1023/A:1020830525823.

[32] Horn, B.K., Schunck, B.G., 1981. Determining optical flow. Artif. Intell. 17, 185–203. doi:https://doi.org/10.1016/0004-3702(81)90024-2.

[33] Hsiao, H.Y., Hsieh, C.Y., Chen, X., Gong, Y., Luo, X., Liao, G., 2014. New development of nonrigid registration. ANZIAM J. 55, 289–297. doi:https://doi.org/10.1017/S1446181114000091.

[34] Hsieh, H.W., Charon, N., 2021. Diffeomorphic registration with density changes for the analysis of imbalanced shapes, in: Lect. Notes Comput. Sci., pp. 31–42. doi:https://doi.org/10.1007/978-3-030-78191-0_3.

[35] Hömke, L., Frohn-Schauf, C., Henn, S., Witsch, K., 2007. Total variation based image registration, in: Image. Process. Partial. Differ. Equ., pp. 343–361. doi:https://doi.org/10.1007/978-3-540-33267-1_19.

[36] Joshi, S., Miller, M., 2000. Landmark matching via large deformation diffeomorphisms. IEEE Trans. Image Process. 9, 1357–1370. doi:https://doi.org/10.1109/83.855431.

[37] Köstler, H., Ruhnau, K., Wienands, R., 2008. Multigrid solution of the optical flow system using a combined diffusion- and curvature-based regularizer. Numer. Linear Algebra Appl. 15, 201–218. doi:https://doi.org/10.1002/nla.576.

[38] Lam, K.C., Lui, L.M., 2014. Landmark- and intensity-based registration with large deformations via quasi-conformal maps. SIAM J. Imaging Sci. 7, 2364–2392. doi:https://doi.org/10.1137/130943406.

[39] Lam, K.C., Lui, L.M., 2015. Quasi-conformal hybrid multi-modality image registration and its application to medical image fusion, in: Adv. Vis. Comput., Cham. pp. 809–818. doi:https://doi.org/10.1007/978-3-319-27857-5_72.

[40] Lombaert, H., Grady, L., Pennec, X., Ayache, N., Cheriet, F., 2013. Spectral log-demons: Diffeomorphic image registration with very large deformations. Int. J. Comput. Vis. 107, 254–271. doi:https://doi.org/10.1007/s11263-013-0681-5.

[41] Mang, A., Ruthotto, L., 2017. A Lagrangian Gauss–Newton–Krylov solver for mass- and intensity-preserving diffeomorphic image registration. SIAM J. Sci. Comput. 39, B860–B885. doi:https://doi.org/10.1137/17M1114132.

[42] Modersitzki, J., 2009. FAIR: Flexible Algorithms for Image Registration. SIAM. doi:https://10.1137/1.9780898718843.

[43] Mok, T.C., Chung, A.C., 2020. Fast symmetric diffeomorphic image registration with convolutional neural networks doi:https://doi.org/10.1109/CVPR42600.2020.00470.

[44] Moore, C.S., Liney, G.P., Beavis, A.W., 2004. Quality assurance of registration of CT and MRI data sets for treatment planning of radiotherapy for head and neck cancers. J. Appl. Clin. Med. Phys. 5, 25–35. doi:https://doi.org/10.1120/jacmp.v5i1.1951.

[45] Nocedal, J., Wright, S., 2006. Numerical Optimization. 2nd ed., Oxford University Press, New York.

[46] Risser, L., Vialard, F., Wolz, R., Murgasova, M., Holm, D.D., Rueckert, D., 2011. Simultaneous multi-scale registration using large deformation diffeomorphic metric mapping. IEEE T. Med. Imaging 30, 1746–1759. doi:https://doi.org/10.1109/TMI.2011.2146787.

[47] Ruhaak, J., Polzin, T., Heldmann, S., Simpson, I.J.A., Handels, H., Modersitzki, J., Heinrich, M.P., 2017. Estimation of large motion in lung CT by integrating regularized keypoint correspondences into dense deformable registration. IEEE T. Med. Imaging 36, 1746–1757. doi:https://doi.org/10.1109/TMI.2017.2691259.

[48] Thirion, J.P., 1998. Image matching as a diffusion process: an analogy with Maxwell's demons. Med. Image. Anal. 2, 243–260. doi:https://doi.org/10.1016/S1361-8415(98)80022-4.

[49] Trottenberg, U., Oosterlee, C.W., Schuller, A., 2001. Multigrid. Academic Press.

[50] Vercauteren, T., Pennec, X., Perchant, A., Ayache, N., 2008. Symmetric log-domain diffeomorphic registration: A demons-based approach, in: Med. Image Comput. Comput. Assist. Interv. 2008, pp. 754–761. doi:https://doi.org/10.1007/978-3-540-85988-8_90.

[51] Wei, D., Ahmad, S., Guo, Y., Chen, L., Huang, Y., Ma, L., Wu, Z., Li, G., Wang, L., Lin, W., Yap, P.T., Shen, D., Wang, Q., 2022. Recurrent tissue-aware network for deformable registration of infant brain MR images. IEEE T. Med. Imaging 41, 1219–1229. doi:https://doi.org/10.1109/TMI.2021.3137280.

[52] Yanovsky, I., Guyader, C.L., Leow, A., Toga, A.W., Thompson, P.M., Vese, L., 2008. Unbiased volumetric registration via nonlinear elastic regularization, in: 2nd MICCAI workshop Math. Found. Comput. Anat.

[53] Yanovsky, I., Osher, S., Thompson, P.M., Leow, A.D., 2007. Log-unbiased large-deformation image registration, in: 2nd Int. Conf. Comput. Vis. Theory Appl.

[54] Yeo, B., Sabuncu, M., Vercauteren, T., Ayache, N., Fischl, B., Golland, P., 2010. Spherical demons: Fast diffeomorphic landmark-free surface registration. IEEE T. Med. Imaging 29, 650–668. doi:https://doi.org/10.1109/TMI.2009.2030797.

[55] Zeidler, E., 1985. Nonlinear Functional Analysis and its Applications III: Variational Methods and Optimization. Springer-Verlag.

[56] Zhang, D., Chen, K., 2018. A novel diffeomorphic model for image registration and its algorithm. J. Math. Imaging Vis. 60, 1261–1283. doi:https://doi.org/10.1007/s10851-018-0811-3.

[57] Zhang, D., Choi, G.P.T., Zhang, J., Lui, L.M., 2022. A unifying framework for n-dimensional quasi-conformal mappings. SIAM J. Imaging Sci. 15, 960–988. doi:https://doi.org/10.1137/21M1457497.

[58] Zhang, J., Chen, K., 2015. Variational image registration by a total fractional-order variation model. J. Comput. Phys. 293, 442–461. doi:https://doi.org/10.1016/j.jcp.2015.02.021.

[59] Zhang, J., Chen, K., Yu, B., 2016. An improved discontinuity-preserving image registration model and its fast algorithm. Appl. Math. Model. 40, 10740–10759. doi:https://doi.org/10.1016/j.apm.2016.08.009.

[60] Zhang, J., Li, Y., 2021. Diffeomorphic image registration with an optimal control relaxation and its implementation. SIAM J. Imaging Sci. 14, 1890–1931. doi:https://doi.org/10.1137/21M1391274.

[61] Zhang, J., Sun, Z., Kong, X., Zhang, J., . A vectorial minimized surface regularizer based image registration model and its numerical algorithm. Appl. Math. Model. 106, 150–176. doi:https://doi.org/10.1016/j.apm.2022.01.015.